NATIONAL ADVISORY COMMITTEE FOR AERONAUTICS

TECHNICAL NOTE 4113

STUDY OF PRESSURE DISTRIBUTIONS ON SIMPLE

SHARP-NOSED MODELS AT MACH NUMBERS

FROM 16 TO 18 IN HELIUM FLOW

By Wayne D. Erickson

Langley Aeronautical Laboratory
Langley Field, Va.

Washington

October 1957

G

NATIONAL ADVISORY COMMITTEE FOR AERONAUTICS

TECHNICAL NOTE 4113

STUDY OF PRESSURE DISTRIBUTIONS ON SIMPLE

SHARP-NOSED MODELS AT MACH NUMBERS

FROM 16 TO 18 IN HELIUM FLOW

By Wayne D. Erickson

SUMMARY

Pressure distributions on some simple sharp-nosed aerodynamic shapes have been obtained at Mach numbers from 16 to 18 in helium flow. The results obtained for the flat plate differ from the prediction of Lees for the strong interaction region by an amount which may be accounted for by the finite thickness of the leading edge. The wedge results are believed to be influenced by a bleedoff effect which results in a lower surface pressure than predicted by the viscous-interaction theory. The results for the 5° and 10° cones show better agreement with the Taylor-Maccoll prediction as the cone angle becomes larger. Temperature recovery factors are also presented and agree with the Prandtl number relationship.

INTRODUCTION

The possibility of operating air wind tunnels for long time intervals at Mach numbers above 12 to 14 appears remote, and the use of helium flow to obtain test data and study aerodynamic and viscous effects at Mach numbers approaching satellite velocity has received increased attention. At present there are few data available for Mach numbers above 10.

The primary purpose of this investigation was to obtain pressure-distribution data at Mach numbers ranging from 16 to 18 for some simple sharp-nosed aerodynamic shapes. From these data the accuracy of available theory for predicting pressure distributions may be assessed. In addition, it was desired to show qualitatively the importance of the viscous-compressible effects and to identify those effects that account for the shortcomings of present theory.

Several theoretical studies concerning the viscous-compressible interaction problem have been reported. These studies may be classified into the so-called weak-interaction theory and the strong-interaction theory. Within the strong-interaction region there are two approaches to the

viscous solution. The first approach assumes that two separate regions exist behind the shock: the viscous boundary layer and a zone of inviscid flow between the shock and the edge of the boundary layer. The second approach assumes that only one region exists under the shock; this region is treated by the boundary-layer equations. Reported studies based on the first approach to the strong-interaction region are those by Bertram (ref. 1), Kuo (ref. 2), Lees (refs. 3 and 4), and Lees and Probstein (ref. 5). Investigations which use the second approach are reported by Li and Nagamatsu (ref. 6) and Shen (ref. 7).

Results of experimental investigations on the viscous-compressible effects in air have been reported by Bertram (ref. 8) for a Mach number of 6.9 and by Kendall (ref. 9) for a Mach number of 5.8. Experimental studies in helium flow have been reported by Hammitt and Bogdonoff (refs. 10 and 11) for Mach numbers up to 14.3 and by Munson (ref. 12) for a Mach number of 18.4.

The Mach number range for the present investigation was from 16 to 18, and the flow Reynolds number was from 0.9×10^6 to 1.5×10^6 per inch.

SYMBOLS

C   linear viscosity coefficient in relation $\mu_w/\mu_l = C\left(T_w/T_l\right)$

and determined from relation $C = \left(1 + \dfrac{\gamma - 1}{2} M^2\right)^{\omega-1}$, for $N_{Pr} = 1$

d   diameter

h   height of model

l length of model

M   Mach number

p   pressure

p_b back pressure

Δp induced static pressure, measured surface pressure minus inviscid pressure

N_{Pr} Prandtl number

R   Reynolds number

r   radius

t   leading-edge thickness

T   absolute temperature

w   width of model

x_{le} distance from leading edge of model

x_{th} distance from throat of nozzle

y   lateral distance from center line of nozzle

γ ratio of specific heats

μ viscosity

$\overline{\chi}$ hypersonic interaction parameter, $M_l^3 \sqrt{C} / \sqrt{R_{x,l}}$

ω viscosity power law index in relation $\mu_w / \mu_l = \left(T_w / T_l\right)^\omega$

Subscripts:

o   stagnation condition

le   leading-edge condition

t   factor based on leading-edge thickness

x   factor based on distance from leading edge

w   wall condition

l   local inviscid condition

∞ free-stream condition

Superscript:

'   total-pressure condition

APPARATUS

All tests were performed in a small-scale hypersonic helium tunnel located in the Langley 9-Inch Tunnel Section. This tunnel is shown in figure 1. The tunnel has a throat diameter of 0.030 inch and expands with a divergence angle of 5° to a constant-area section which is 0.907 inch in diameter. Helium was supplied from a 55-cubic-foot reservoir to the tunnel stagnation chamber at pressures up to 3,000 pounds per square inch. Under these conditions, the tunnel could be operated for 20 minutes at a stagnation pressure of 2,400 pounds per square inch. A two-stage steam ejector was used to maintain a back pressure as low as 0.75 pound per square inch absolute depending on the mass flow of helium. The stagnation temperature for any given test was constant and always in the range of 85° F to 95° F. In order to facilitate the study of back-pressure effects, a control valve was located just downstream of the tunnel exhaust.

This tunnel was equipped with removable schlieren windows and corresponding contoured inserts. The schlieren windows disturbed the axisymmetric feature of the nozzle shape and were inserted only for optical observations. The contoured inserts which replaced the schlieren windows retained the axisymmetric feature and were used for all pressure and temperature studies.

The test models were supported by means of a long sting as shown in figure 1. The sting was positioned by a motorized gear-and-screw system and centered with a spider and bushing located just downstream of the tunnel exhaust. The orifice locations and dimensions of the test models are shown in figure 2. The orifices were all 0.015 inch in diameter. For the models on which temperatures were measured, the thermocouple junctions were located at positions which correspond to the orifice locations.

TUNNEL CALIBRATION

The design expansion ratio of the tunnel corresponds to a Mach number of 24.4 based on one-dimensional theory. (See fig. 3.) However, the Mach number obtained from a total-pressure survey was considerably less than that predicted by one-dimensional theory, as shown in figure 3. The total pressures were measured for the stagnation pressures of 2,000, 2,400, and 2,800 pounds per square inch at 0.5-inch intervals between 4.5 and 6.0 inches from the nozzle throat. These intervals corresponded to the locations of the schlieren windows. For the entire calibration, the contoured inserts were used to retain the axisymmetric feature of the nozzle. The Mach number gradient along the center line of the nozzle, which is shown in figure 3, is of the order of 2 per inch between 4.5 and 5.0 inches from the throat, while the gradient is less farther downstream. Between 5.5 and 6.0 inches from the throat the gradient is approximately 1 per inch. The effect of stagnation pressure on Mach number is also

shown in figure 3. As the stagnation pressure increases, the Mach number increases. This variation might be expected since a reduction in the wall boundary-layer thickness allows a relatively greater flow cross-sectional area. This effect is slight at the 4.5- and 5.0-inch locations, but a large effect is shown at the 5.5- and 6.0-inch locations.

A lateral total-pressure survey for stagnation pressures of 2,000, 2,400, and 2,800 pounds per square inch at a constant back pressure of 1 pound per square inch absolute was made to determine the useful testing region of the tunnel. The results of this survey are given in figure 4. Figure 4 shows that the useful free-stream core is approximately 0.4 inch in diameter. The lateral Mach number distributions for the various stagnation pressures are shown in figure 5. The Mach number variation at 4.5 and 5.0 inches from the throat is ±1 percent in the useful testing region and somewhat greater at the more downstream positions.

A lateral total-pressure survey was also made for various back pressures and a constant stagnation pressure to determine the effect of back pressure on the quality of the flow. The stagnation pressure was held constant at 2,400 pounds per square inch while tests were made at back pressures of 1.0, 1.5, and 2.0 pounds per square inch absolute. Figure 6 shows the results of these tests. In figure 6 the ratio of total pressure to stagnation pressure is plotted against lateral distance from the tunnel center line at various distances from the nozzle throat. Figure 7 presents these same data in terms of free-stream Mach number.

Figure 6 shows that, at a distance of 4.5 inches from the throat, the back pressure does not affect the total-pressure measurements. The lateral survey at 5.0 inches from the throat indicates negligible effect of back pressure for values of 1.0 and 1.5 pounds per square inch absolute; however, when the back pressure is raised to 2.0 pounds per square inch absolute, the adverse effect of increasing back pressure becomes very noticeable. The change in Mach number caused by this increase in back pressure is shown in figure 7. The effect of back pressure becomes even greater at the 5.5- and 6.0-inch locations.

PRECISION

The estimated probable error for the measurement of the stagnation pressure is ±5 pounds per square inch and that for the total pressure is ±0.1 pound per square inch. This combination of errors gives an accuracy of approximately ±0.3 percent in Mach number for the range from 16 to 18 at stagnation pressures of 2,000 to 2,800 pounds per square inch. The estimated accuracy in measuring the surface pressure on the test models is ±0.008 pound per square inch. The magnitude of the estimated error for the ratios p/p_0 and $\Delta p/p_l$ is given in the following table for the various test models for $p_0 = 2,400$ pounds per square inch and $M_{le} = 17.3$:

Configuration	p/p_o	$\Delta p/p_l$
Flat plate	$\pm 0.03 \times 10^{-4}$	± 0.3
5° wedge	$\pm.03$	$\pm.05$
10° wedge	$\pm.03$	$\pm.015$
5° cone	$\pm.03$	$\pm.06$
10° cone	$\pm.03$	$\pm.018$

The measured temperatures are estimated to be accurate within $\pm 1^\circ$ F.

TESTS

For all the tests, the models were alined along the tunnel center line at zero angle of attack and zero angle of yaw. The tunnel back pressure was held to less than 1 pound per square inch absolute for all tests. The free-stream Mach number was varied by changing the longitudinal location of the models. Figure 3 shows the free-stream Mach number plotted against distance from the throat of the tunnel. The Mach number at the leading edge of the test models was in the range from 16.0 to 17.4. The Reynolds number was varied by changing the stagnation pressure within the limits 2,000 to 2,800 pounds per square inch. The viscosity-temperature relationship reported by Akin (ref. 13) is

$$\mu = 8.315 T^{0.647} \times 10^{-4}$$

where μ is the viscosity in lb/hr-ft and T is in $^\circ$R. This relationship was used in the Reynolds number determination. Figure 8 shows the free-stream test Reynolds numbers to be in the range from 0.9×10^6 to 1.5×10^6 per inch. The Reynolds number based on leading-edge thickness R_t for each model was determined and all values indicate continuum flow. The numerical values of R_t are presented along with the pressure-distribution results. The surface static pressures on each model were measured at the settled-out condition which was usually obtained after 3 to 4 minutes. The surface temperatures on the two-dimensional models were also obtained and required 2 to 3 minutes to reach equilibrium.

RESULTS AND DISCUSSION

Temperature Recovery

In order to determine the validity of the assumption that the models were tested under adiabatic conditions, temperature recovery factors were obtained on the two-dimensional shapes. These factors are shown in figure 9. With a constant Prandtl number N_{Pr}, the theoretical recovery factor for a laminar boundary layer is $N_{Pr}^{1/2}$ (ref. 14). A representative Prandtl number for helium is 0.695 (refs. 13, 15, and 16). The recovery factor calculated from $N_{Pr}^{1/2}$ is therefore approximately 0.83. The measured temperature recovery factors shown in figure 9 range approximately from 0.83 to 0.88. For the flat plate, the temperature recovery factors are highest near the leading edge and decrease with distance downstream from the leading edge. This temperature gradient is possibly due to heat transfer from the lower surface or wedge-shape portion through the plate to the upper surface where the thermocouples are located. This comparison of figure 9 with the Prandtl number relation indicates that essentially insulated conditions existed on the models during the tests.

Schlieren Observations

Schlieren photographs were obtained for all test models at the two test locations which correspond to leading-edge Mach numbers of 16.1 and 17.3. Figure 10 shows a strong shock over the upper surface of the flat plate. This shock is believed to be generated by the boundary layer on the plate since the boundary layer causes an effective model thickness and a probable contribution due to the finite leading edge. Figure 10 also shows the close proximity of the shock wave to the boundary layer near the leading edges of the wedges and cones.

Pressure Distribution

Flat plate.- The pressure distribution along the surface of a flat plate is shown in figure 11. The ratio of measured surface static pressure to stagnation pressure is plotted against the distance from the leading edge and compared with the calculated inviscid-pressure ratio. Since there is an appreciable Mach number gradient in the tunnel, the inviscid pressure and Mach number were calculated for local conditions based on this gradient which was determined from a tunnel calibration with no model but at corresponding orifice locations. The inviscid ratio of p/p_0 is shown in figure 11 for $M_{le} = 16.1$ and 17.3.

Figure 11 indicates that the measured surface pressures are from 9 to 10 times the inviscid pressure at a location 0.051 inch from the

leading edge and decrease to 5 or 6 times the inviscid pressure at
0.304 inch.

The induced-pressure increment divided by the inviscid pressure is
plotted against $1/\sqrt{R_{x,l}}$ in figure 12, where $R_{x,l}$ is the local Reynolds
number based on the distance from the leading edge. The significance of
this correlation is better understood when it is remembered that the local
streamline deflection induced by the boundary layer is of the order
$1/\sqrt{R_{x,l}}$. The data plotted in this manner form an essentially straight
line for a given Mach number. However, the data for $M_{l_e} = 17.3 \pm 0.1$
form a distinctly higher curve than the data form for $M_{l_e} = 16.1 \pm 0.2$.
This difference is due to the greater boundary-layer effects at the higher
Mach number. The data which correspond to the greatest distances from the
leading edge or smallest values of $1/\sqrt{R_{x,l}}$ tend to rise above the trend
established by the more forward locations. This rise in pressure may be
due to a pressure bleed-in to the upper surface from the high-pressure
region at the under surface of the plate or possibly to transition of the
boundary layer.

For the region very close to the leading edge, where the shock—
boundary-layer interaction is strong, the form of the equation for calcu-
lating the induced pressure on an insulated flat plate as set forth by
Lees (ref. 4) is

$$\frac{p}{p_\infty} = A\bar{X}_\infty \tag{1}$$

where $\bar{X}_\infty = M_\infty^3\sqrt{C}/\sqrt{R_{x,\infty}}$ and $A = 0.92$ for helium. For a flat plate,
the local free-stream condition is identical to the local inviscid con-
dition. This equation may therefore be rewritten as

$$\frac{\Delta p}{p_l} = 0.92\bar{X} - 1 \tag{2}$$

and is the zero-order prediction for the induced pressure in the strong-
interaction region.

At greater distances from the leading edge of a flat plate the shock—
boundary-layer interaction is weak. Lees and Probstein (ref. 5) give a
second-order solution for the weak-interaction region for helium flow as

$$\frac{\Delta p}{p_l} = 0.629\overline{X} + 0.152\overline{X}^2 \tag{3}$$

Results for the flat plate are shown in figure 13 where $\Delta p/p_l$ is plotted against $\overline{X}$. A comparison is made with the zero-order strong-interaction theory and the second-order weak-interaction theory. The data corresponding to $\overline{X} > 5$ tend to aline parallel to and somewhat higher than data predicted by the strong-interaction theory, as shown in figure 13. For $\overline{X} < 5$, the induced pressures rise above the established trend because of what is believed to be a pressure bleed effect from the under surface of the plate. The second-order weak-interaction theory should not be applied for values of $\overline{X}$ greater than 2 or 3.

The difference between experiment and the zero-order strong-interaction theory is believed to be due to finite leading-edge effects. Cheng and Pallone (ref. 17) present an equation for predicting the induced-pressure increase due to a finite leading-edge thickness. The induced pressure due to a finite leading edge in helium flow is

$$\Delta\left(\frac{\Delta p}{p_l}\right) = 0.169 k^{2/3} M_\infty^2 \left(\frac{x}{t}\right)^{-2/3} \tag{4}$$

where k is the nose drag coefficient which may be calculated from the following expression (ref. 4):

$$k = c_{p,max} = \frac{\gamma + 3}{\gamma + 1}\left[1 - \frac{2}{(\gamma + 3)M_\infty^2}\right] \tag{5}$$

The following table, based on equations (4) and (5), shows the induced-pressure rise due to the leading-edge thickness of $t = 0.0006$:

Orifice location, x, in.	$\Delta\left(\dfrac{\Delta p}{p_l}\right)$	
	$M_\infty = 17.3$	$M_\infty = 16.1$
0.051	3.8	3.3
.106	2.3	2.0
.237	1.4	1.2
.304	1.2	1.0

These calculated values for $\Delta\left(\dfrac{\Delta p}{p_l}\right)$ indicate that the difference between experiment and zero-order strong-interaction theory shown in figure 13 may be accounted for by the finite leading edge.

Wedges.- Pressure-distribution results for the 5° wedge are presented in figure 14, where the ratio p/p_0 is plotted against the distance from the leading edge. Figures 15 and 16 show these same results with $\Delta p/p_l$ plotted against $1/\sqrt{R_{x,l}}$ and $\overline{X}$, respectively. The results for the 10° wedge are plotted in the same manner in figures 17 to 19.

Figure 14 shows the relation between the measured surface static pressure and the calculated inviscid pressure. Figure 15 shows that $\frac{1}{\sqrt{R_{x,l}}}$ correlates the pressure data fairly well, but there is a distinct definition between the data at $M_{l_e} = 17.3 \pm 0.1$ and $M_{l_e} = 16.1 \pm 0.2$. The data for the higher Mach number indicate a greater induced pressure due to a greater boundary-layer effect. The curve defined by the data should pass through the origin, since as $R_{x,l} \rightarrow \infty$ the induced pressure becomes zero; however, as shown in figure 15, the measured surface static pressure is tending toward a value less than the calculated inviscid pressure based on a 10° flow-deflection angle at each orifice. This trend is likely due to a pressure bleedoff from the model surface to the low stream pressure which exists adjacent to the parallel sides of the wedge or to the low-pressure region at the base of the wedge or to both regions.

The equation for predicting the induced pressure on a wedge in the weak-interaction region is identical to the equation for a flat plate in the weak-interaction region if $\overline{X}$ is evaluated for the local conditions. Equation (3), then, represents the second-order weak-interaction theory for the wedges.

Figure 16 shows that the data corresponding to values of $0.8 \leqq \overline{X} \leqq 1.2$ fall somewhat below but parallel to the second-order weak-interaction theory. For values of $\overline{X} < 0.8$, the data depart from prediction to an even greater extent. It is believed that the entire surface of the wedge is influenced by a bleedoff to the parallel edges. In addition, the greater departure from theory at the more rearward orifices may be due to the additional bleedoff to the low-pressure region at the base of the wedge.

Figure 17 shows that the measured surface pressures on the 10° wedge are less than those predicted by two-dimensional inviscid theory under certain conditions, possibly because of the actual three-dimensional effects which allow a pressure bleedoff to the parallel sides and to the low-pressure region at the base of the wedge. Figure 19 shows that the results for $M_{l_e} = 17.3 \pm 0.1$ and for $M_{l_e} = 16.1 \pm 0.2$ tend to form two separate curves but differ in magnitude by only twice the estimated accuracy for $\Delta p/p_l$. Aside from this small difference, the results for the 10° wedge presented in figure 19 show that the $\overline{X}$ parameter correlates the data in spite of the obviously large bleedoff effects.

Cones.- Pressure-distribution results for the 5° cone are presented in figure 20, where the ratio p/p_O is plotted against the distance from the leading edge. The same data are represented in figures 21 and 22, where $\Delta p/p_l$ is plotted against $1/\sqrt{R_{x,l}}$ and $\overline{X}$, respectively. The results for the 10° cone are represented in a similar manner in figures 23 to 25.

The results shown in figure 20 for the 5° cone indicate surface pressures which are slightly higher than the Taylor-Maccoll prediction. Figure 21 shows that the greatest induced pressure was observed at the location nearest the apex for $M_{le} = 17.2$ and was 35 percent greater than the calculated inviscid pressure. For this comparison, the zero axis of the ordinate scale represents the calculated inviscid pressure obtained by the Taylor-Maccoll theory. The difference between experiment and Taylor-Maccoll theory decreases to 10 to 20 percent at the second orifice location. The data representing the most rearward orifice show a higher pressure than that expected from the established trend. The schlieren photographs show that the tunnel boundary layer intersects the model shock near the base of the cone; however, the tunnel boundary layer is believed not to affect the surface pressure at the last orifice, since it is well upstream of the point of intersection. There appears to be no reasonable explanation of the pressure rise in the region of the last orifice.

The expression for calculating the induced pressure on an unyawed cone is of the same form as equation (3). By using the Mangler transformation, the cone prediction is obtained. By replacing $\overline{X}$ with $\overline{X}/\sqrt{3}$ in equation (3), the induced pressure on a cone is determined from the equation:

$$\frac{\Delta p}{p_l} = 0.363\overline{X} + 0.051\overline{X}^2 \tag{6}$$

The experimental scatter shown in figure 22 is of the order of the estimated error with the exception of the values of $\overline{X} < 1.0$.

Figure 23 shows the comparison between the results for a 10° cone and Taylor-Maccoll theory. For some conditions, the measured pressure is less than the Taylor-Maccoll prediction. Figure 24 shows that the results obtained on the 10° cone are all within ±6 or 7 percent of the calculated inviscid pressure (that is, the Taylor-Maccoll prediction). In figure 25, evaluation of the correlation of results with $\overline{X}$ is difficult because the range of $\overline{X}$ examined is small.

The results obtained on the 5° and 10° cones are consistent with the results reported by Munson (ref. 12) insofar as the effect of cone angle is concerned. Munson measured surface static pressures on a 15° and 20° cone in helium at $M_\infty = 18.4$ and found good agreement with the Taylor-Maccoll theory. The results from the present study and those reported by Munson show that the surface static pressure on a cone more nearly agrees with the Taylor-Maccoll theory as the cone angle is increased.

Compilation of results.- Figure 26 represents a composite of results for the flat plate and wedges with $\Delta p/p_l$ plotted against $\overline{X}$. The second-order weak-interaction theory and the zero-order strong-interaction theory are also indicated in figure 26. The difference between experiment and the zero-order strong-interaction theory for the flat plate is probably accounted for by the effect of a finite leading-edge thickness, except for the rear orifices which appear to be affected by pressure bleed-in (probably from the under side), whereas all the wedge results are believed to be influenced by a pressure bleedoff mechanism.

A representative curve of the experimental results of Hammitt and Bogdonoff (ref. 10) at $11.8 < M_{le} < 14.3$ is shown in figure 26 for comparison. The results of Hammitt and Bogdonoff show induced pressures of the order of $2\frac{1}{2}$ times the strong-interaction theory for the flat plate, while the results of the present investigation for smaller leading-edge thicknesses are of the order of $1\frac{1}{4}$ times the strong-interaction theory. When the prediction for the induced-pressure rise due to finite leading edge as presented by Cheng and Pallone (ref. 17) is applied to the results of Hammitt and Bogdonoff, the flat-plate results are still much higher than the results predicted by theory. At present no reason is apparent for the large difference in the two experiments.

CONCLUSIONS

An aerodynamic investigation in the Mach number range from 16 to 18 of a flat plate, 5° wedge, 10° wedge, 5° cone, and 10° cone in helium flow indicates the following conclusions:

1. The induced pressures measured on a flat plate in the present investigation are approximately one-half those reported by Hammitt and Bogdonoff for the same values of the hypersonic interaction parameter. There is no apparent reason for this large difference in the two experiments; however, the pressure-distribution data obtained on a flat plate for the present investigation agree reasonably well with the prediction

of Lees for the strong-interaction region, except for an amount which may be accounted for by the finite thickness of the leading edge.

2. The results obtained from the tests with wedges indicated lower surface pressures than those predicted by viscous interaction theory. This result is believed to be caused by a pressure bleedoff effect to the sides, the edges, and the base.

3. The pressure-distribution results for the cones show increased agreement with the Taylor-Maccoll prediction as the cone angle becomes larger.

4. The measured temperature recovery factors for the two-dimensional models are all approximately equal to the square root of the Prandtl number.

Langley Aeronautical Laboratory,
    National Advisory Committee for Aeronautics,
        Langley Field, Va., July 9, 1957.

REFERENCES

1. Bertram, Mitchel H.: An Approximate Method for Determining the Displacement Effects and Viscous Drag of Laminar Boundary Layers in Two-Dimensional Hypersonic Flow. NACA TN 2773, 1952.

2. Kuo, Y. H.: Viscous Flow Along a Flat Plate Moving at High Supersonic Speeds. Jour. Aero. Sci., vol. 23, no. 2, Feb. 1956, pp. 125-136.

3. Lees, Lester: On the Boundary Layer Equations in Hypersonic Flow and Their Approximate Solutions. Rep. No. 212 (Contract No. AF 33(038)-250), Princeton Univ., Aero. Eng. Lab., Sept. 20, 1952.

4. Lees, Lester: Hypersonic Flow. GALCIT Pub. No. 404, 1955.

5. Lees, Lester, and Probstein, Ronald F.: Hypersonic Viscous Flow Over a Flat Plate. Rep. No. 195, Princeton Univ., Aero. Eng. Lab., Apr. 20, 1952.

6. Li, Ting-Yi, and Nagamatsu, H. T.: Shock Wave Effects on the Laminar Skin Friction of an Insulated Flat Plate at Hypersonic Speeds. GALCIT Memo. No. 9 (Contract No. DA-04-495-Ord-19), July 1, 1952.

7. Shen, Shan-Fu: An Estimate of Viscosity Effect on the Hypersonic Flow Over an Insulated Wedge. Jour. Math. and Phys., vol. XXXI, no. 3, Oct. 1952, pp. 192-205.

8. Bertram, Mitchel H.: Viscous and Leading-Edge Thickness Effects on the Pressures on the Surface of a Flat Plate in Hypersonic Flows. Jour. Aero. Sci. (Readers' Forum), vol. 21, no. 6, June 1954, pp. 430-431.

9. Kendall, James M., Jr.: An Experimental Investigation of Leading-Edge Shock-Wave - Boundary-Layer Interaction at Mach 5.8. Jour. Aero. Sci., vol. 24, no. 1, Jan. 1957, pp. 47-56.

10. Hammitt, A. G., and Bogdonoff, S. M.: A Study of the Flow About Simple Bodies at Mach Numbers From 11 to 15. WADC Tech. Rep. 54-257, Wright Air Dev. Center, U. S. Air Force, Oct. 1954.

11. Hammitt, A. G., and Bogdonoff, S. M.: Hypersonic Studies of the Leading Edge Effect on the Flow Over a Flat Plate. Jet Propulsion, vol. 26, no. 4, Apr. 1956, pp. 241-246, 250.

12. Munson, Albert G.: A Preliminary Experimental Investigation of the Flow Over Simple Bodies of Revolution at $M = 18.4$ in Helium. GALCIT Memo. No. 35 (Contract No. DA-04-495-Ord-19), Dec. 15, 1956.

13. Akin, S. W.: The Thermodynamic Properties of Helium. Trans. A.S.M.E.,
    vol. 72, no. 6, Aug. 1950, pp. 751-757.

14. Johnson, H. A., and Rubesin, M. W.: Aerodynamic Heating and Convec-
    tive Heat Transfer - Summary of Literature Survey. Trans. A.S.M.E.,
    vol. 71, no. 5, July 1949, pp. 447-456.

15. Nuttall, R. L.: The NBS-NACA Tables of Thermal Properties of Gases.
    Table 6.39 Helium - Coefficient of Viscosity. National Bur.
    Standards, U. S. Dept. of Commerce, Dec. 1950.

16. Nuttall, R. L.: The NBS-NACA Tables of Thermal Properties of Gases.
    Table 6.42 Helium - Thermal Conductivity. National Bur. Standards,
    U. S. Dept. of Commerce, Dec. 1950.

17. Cheng, H. K., and Pallone, A. J.: Inviscid Leading-Edge Effect in
    Hypersonic Flow. Jour. Aero. Sci. (Readers' Forum), vol. 23, no. 7,
    July 1956, pp. 700-702.
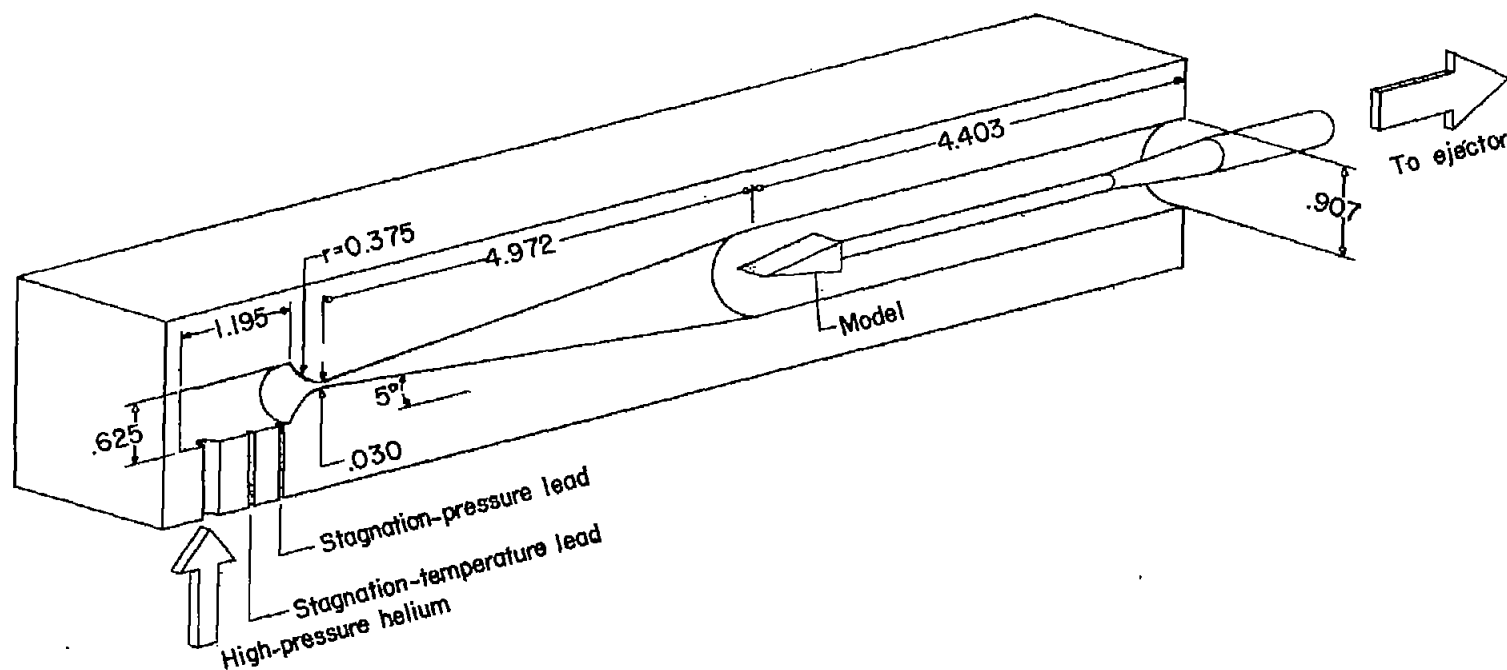
Figure 1.- Sketch of small-scale hypersonic helium tunnel. All dimensions are in inches.
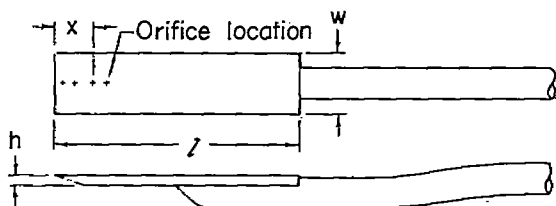
Flat plate:

$x_1 = 0.051$	$l = 1.473$
$x_2 = 0.106$	$h = 0.064$
$x_3 = 0.237$	$w = 0.375$
$x_4 = 0.304$	Leading edge = 0.0006
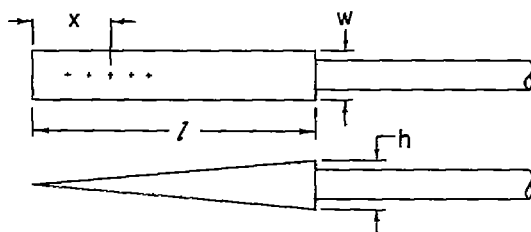
5° wedge:

$x_1 = 0.210$	$l = 1.711$
$x_2 = 0.335$	$h = 0.299$
$x_3 = 0.465$	$w = 0.300$
$x_4 = 0.593$	Leading edge = 0.0007
$x_5 = 0.695$	
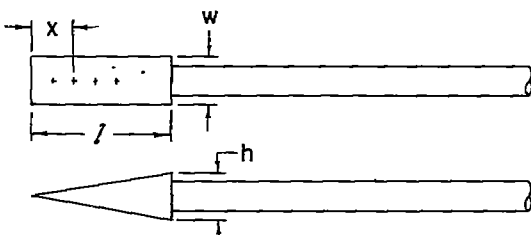
10° wedge:

$x_1 = 0.125$	$l = 0.851$
$x_2 = 0.248$	$h = 0.300$
$x_3 = 0.373$	$w = 0.300$
$x_4 = 0.516$	Leading edge = 0.0005
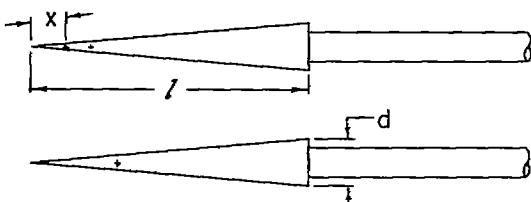
5° cone:

(0°) $x_1 = 0.210$	$l = 1.688$
(180°) $x_2 = 0.356$	$d = 0.297$
(90°) $x_3 = 0.520$	Leading edge = 0.0013
(270°) $x_4 = 0.520$	
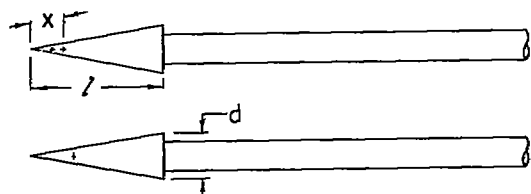
10° cone:

(0°) $x_1 = 0.120$	$l = 0.809$
(180°) $x_2 = 0.185$	$d = 0.296$
(90°) $x_3 = 0.256$	Leading edge = 0.0015
(270°) $x_4 = 0.256$	

Figure 2.- Test models. All dimensions are in inches.
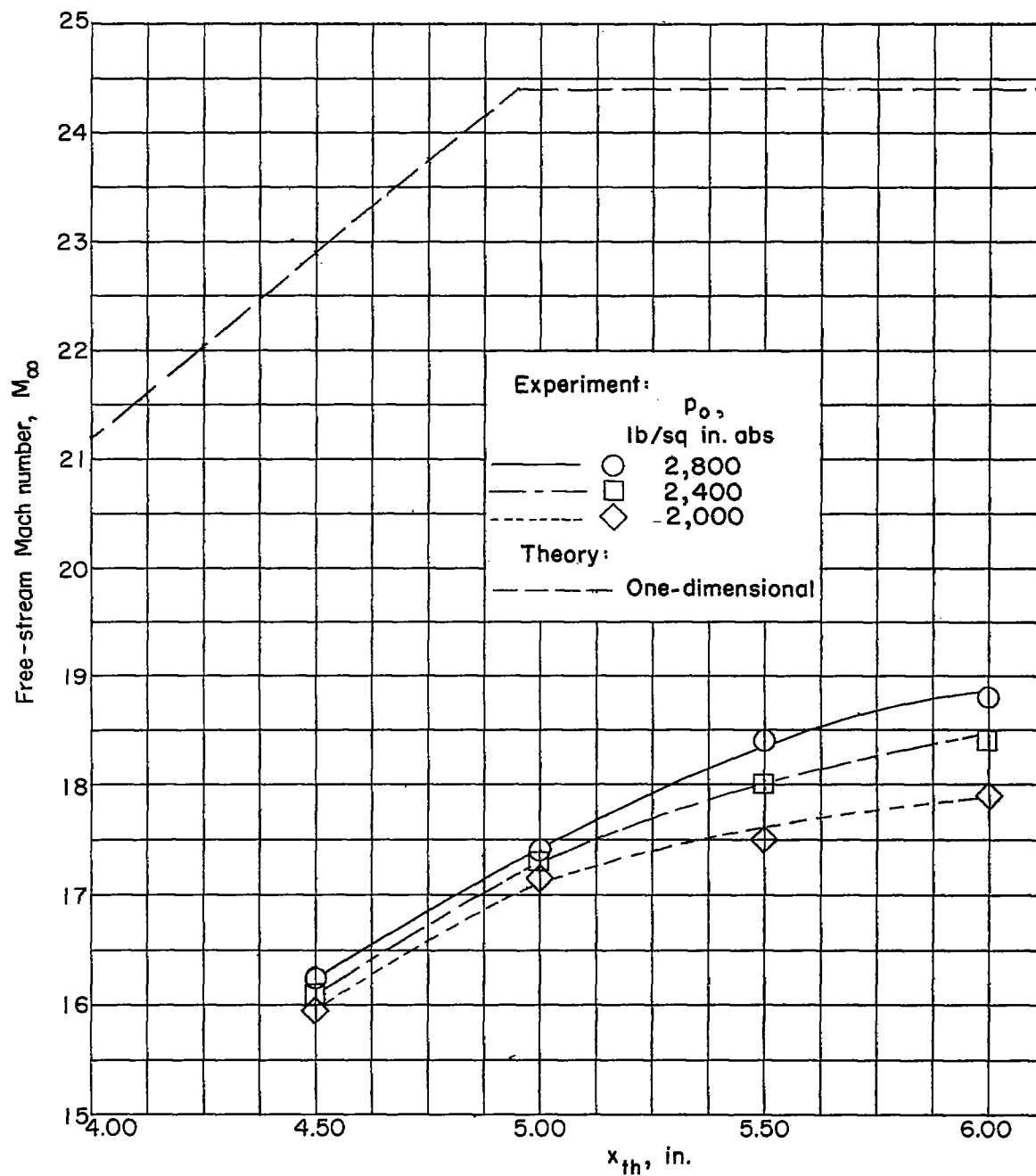
Figure 3.- Mach number distribution along center line of nozzle.
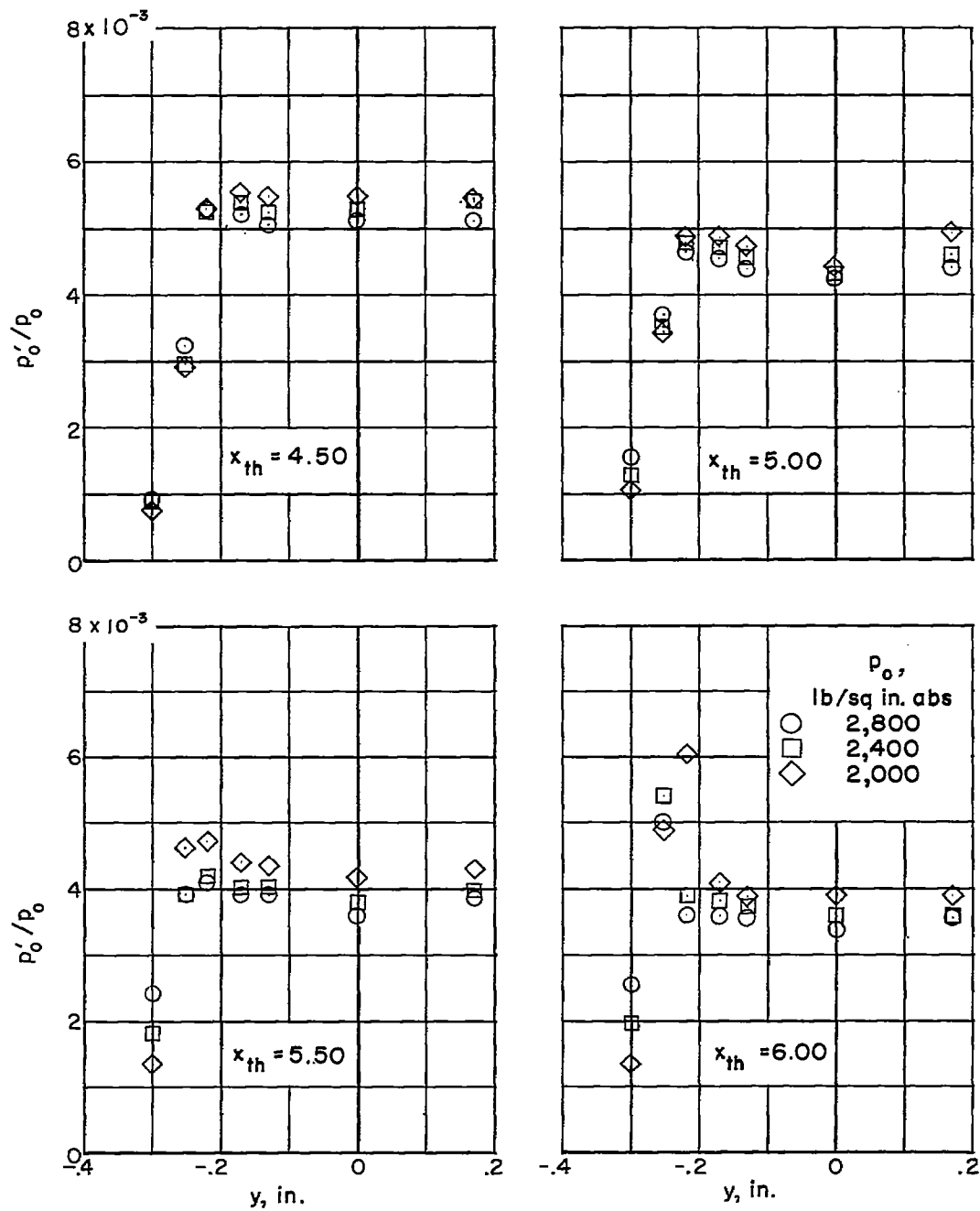
Figure 4.- Lateral total-pressure survey for various stagnation pressures and constant back pressure. p_b = 1.0 pound per square inch absolute.
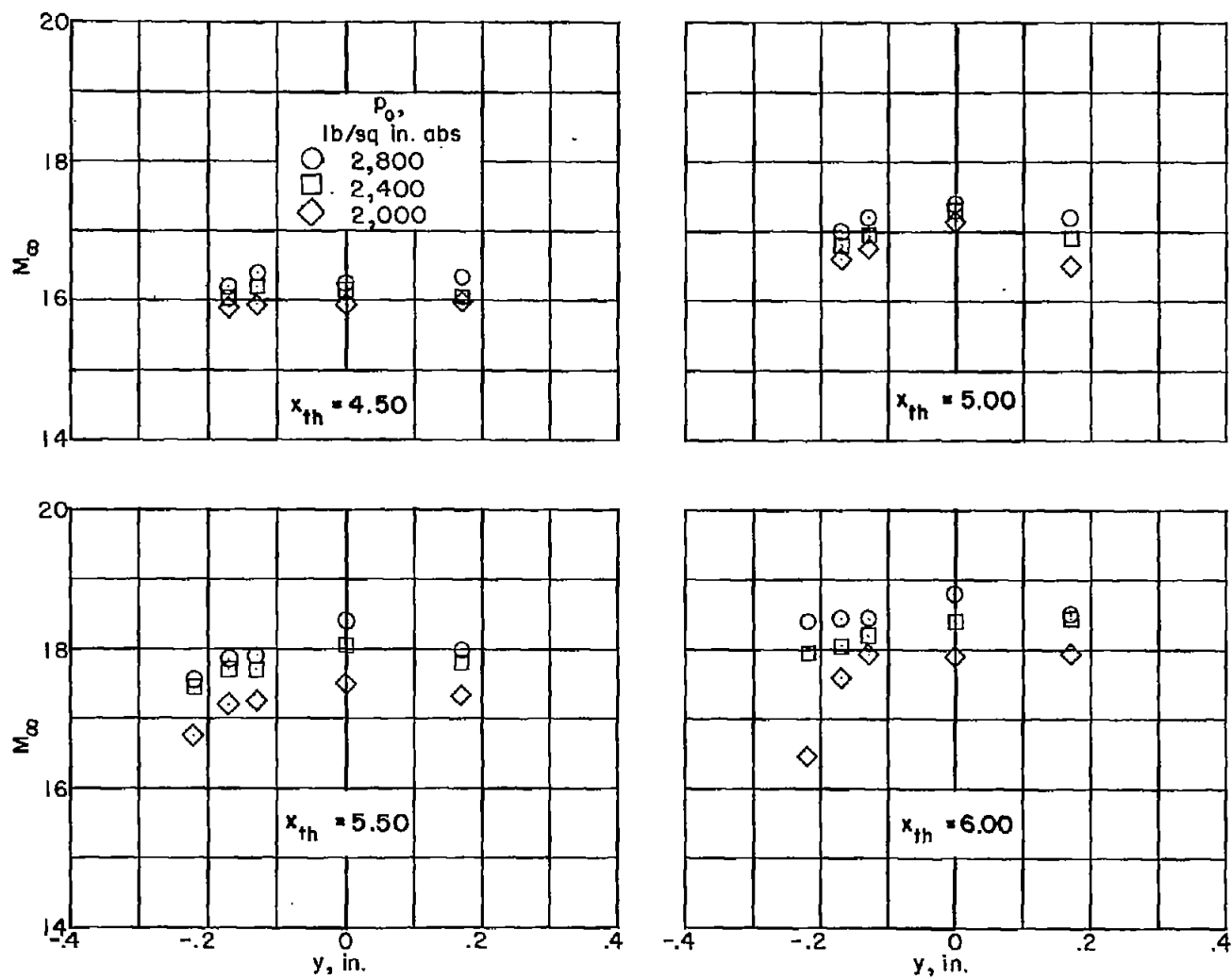
Figure 5.- Lateral Mach number distribution for various stagnation pressures and constant back pressure. p_b = 1.0 pound per square inch absolute.
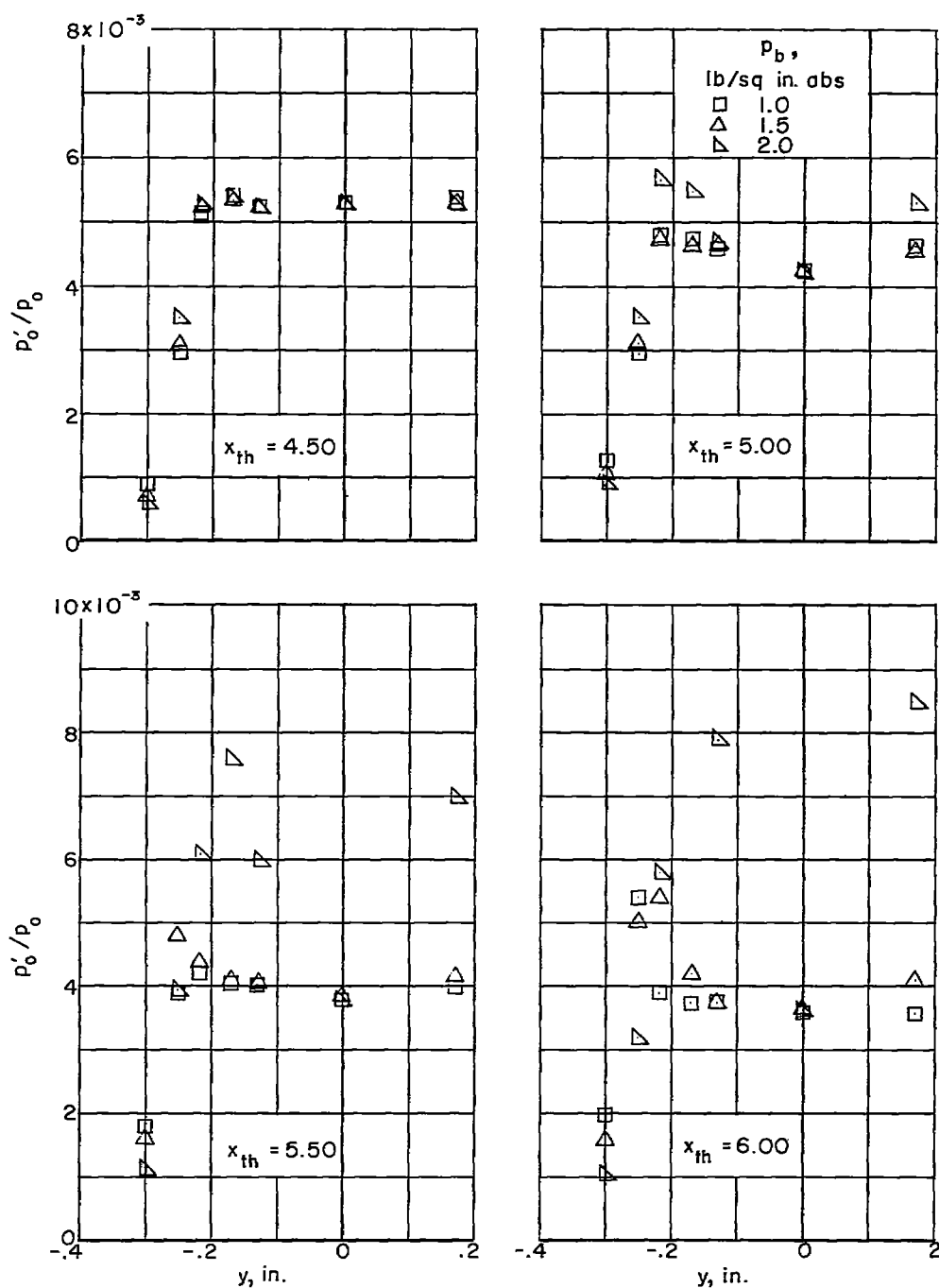
Figure 6.- Lateral total-pressure survey for various back pressures and constant stagnation pressure. $p_o = 2,400$ pounds per square inch absolute.
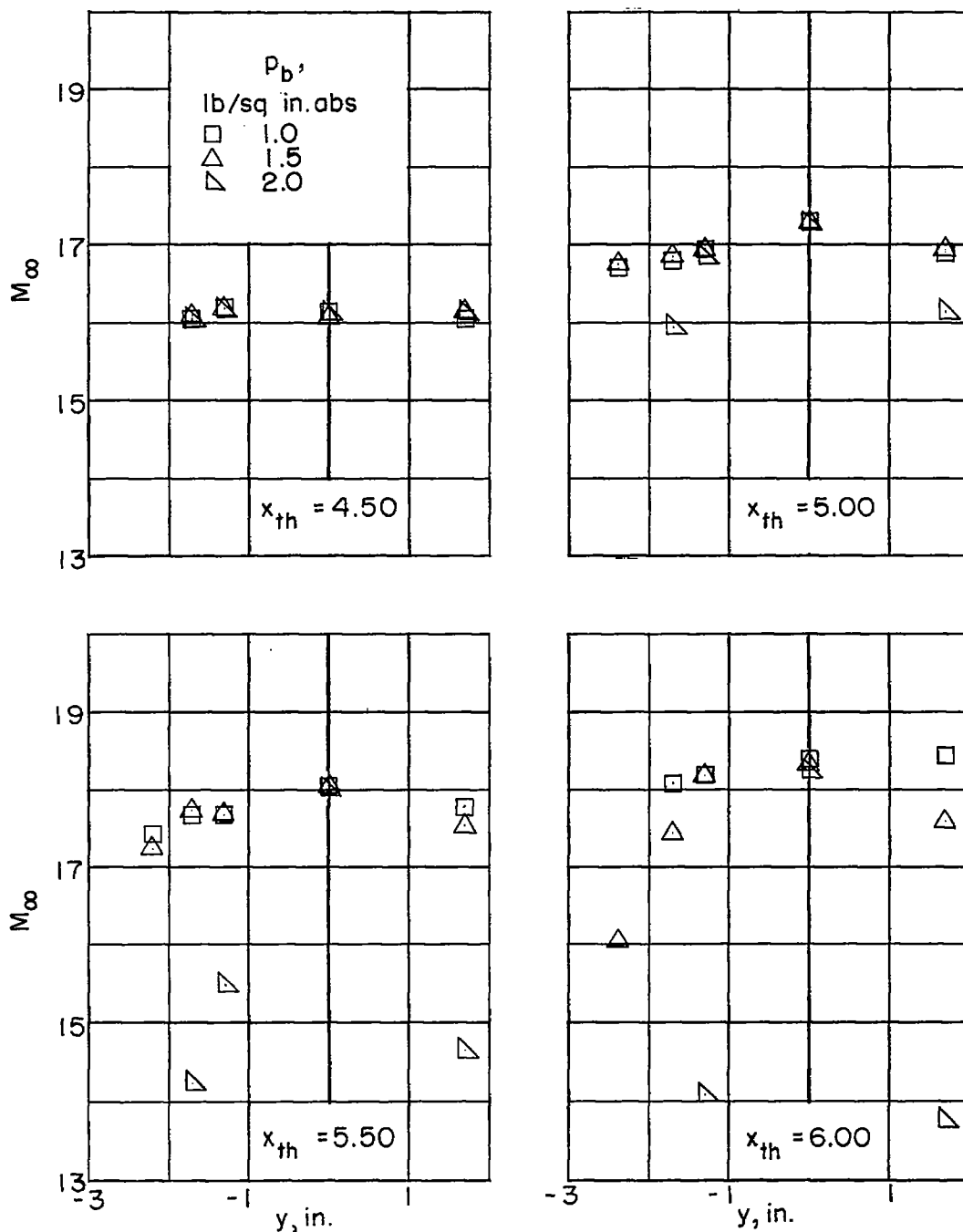
Figure 7.- Lateral Mach number distribution for various back pressures and constant stagnation pressure. p_o = 2,400 pounds per square inch absolute.
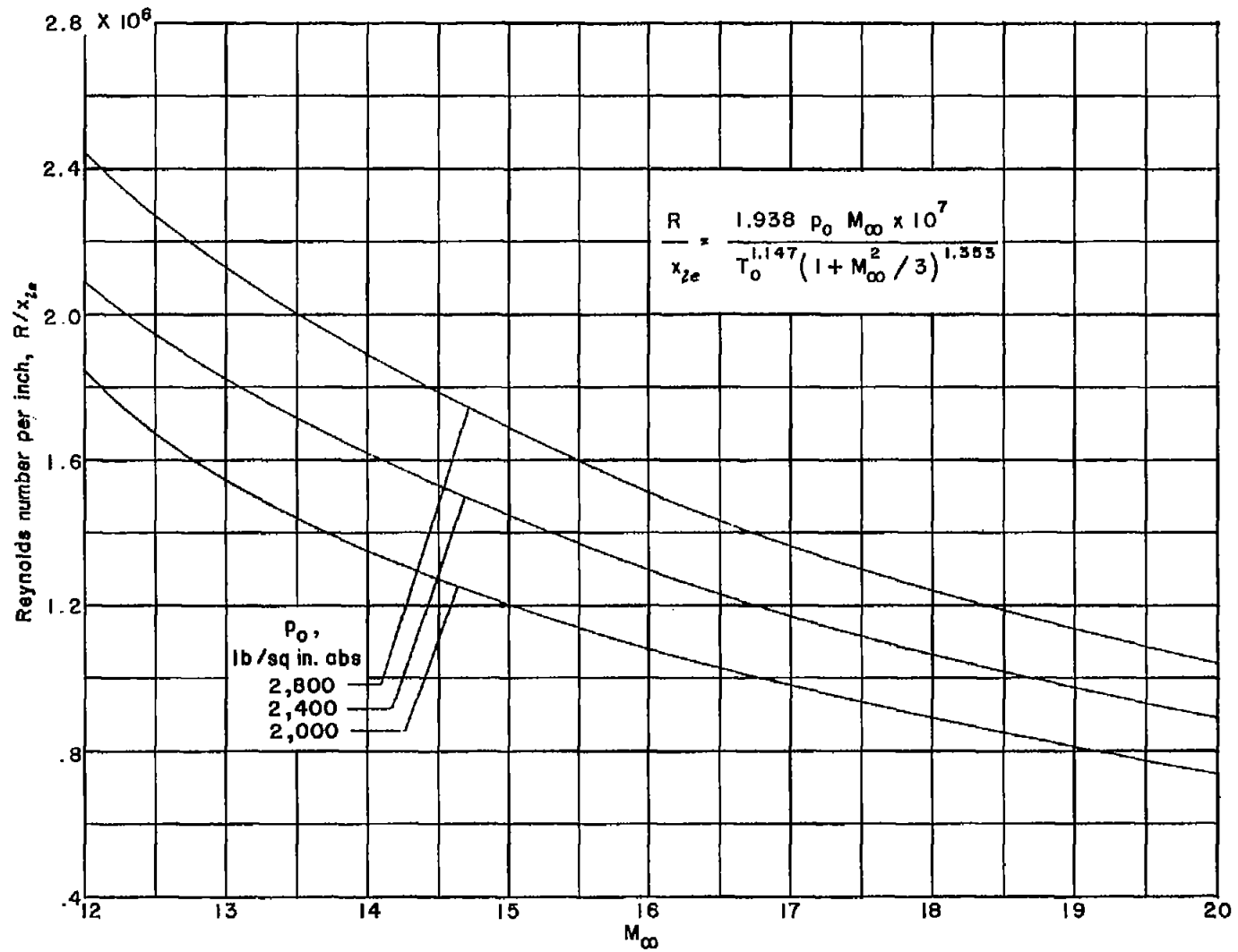
Figure 8.- Variation of Reynolds number with Mach number for various stagnation pressures and constant stagnation temperature. $T_0 = 545^\circ$ R.
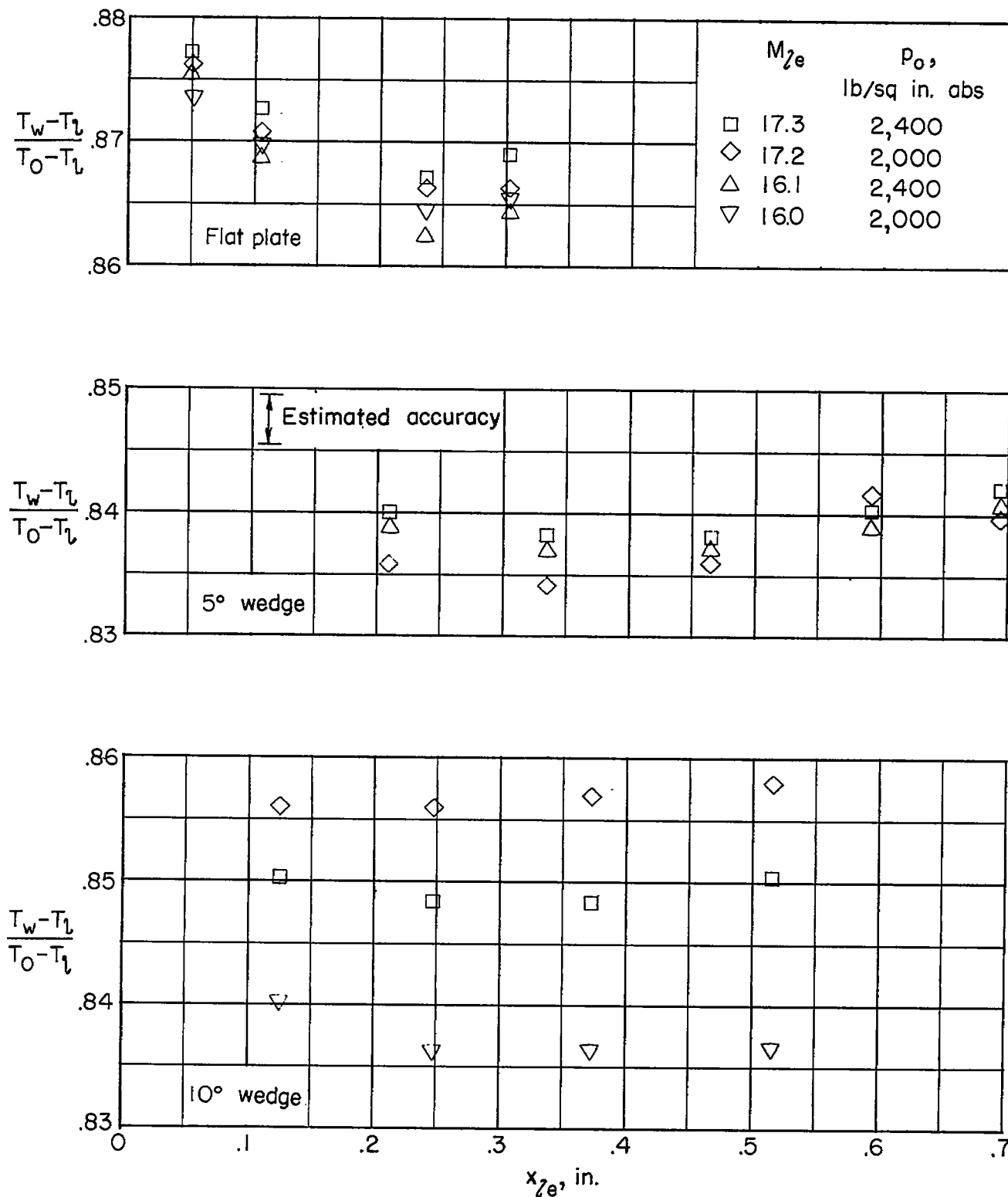
Figure 9.- Variation of temperature recovery factor with distance from leading edge for flat plate, 5° wedge, and 10° wedge. $T_o = 555^\circ$ R.

Flat plate
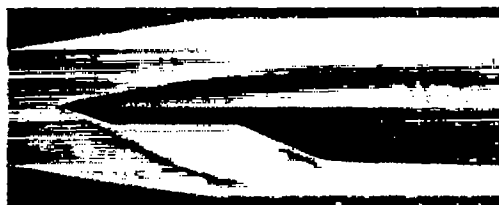
5° wedge
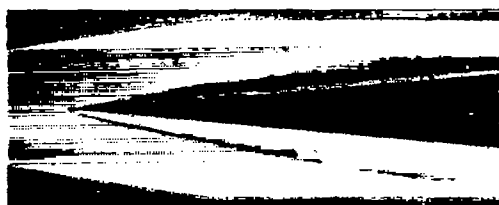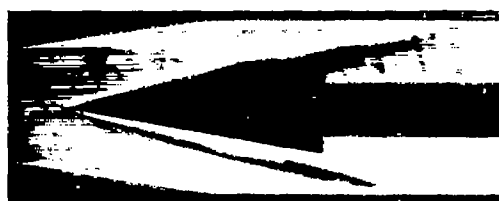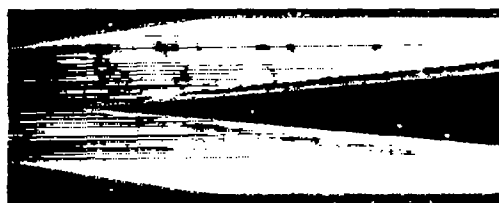
10° wedge
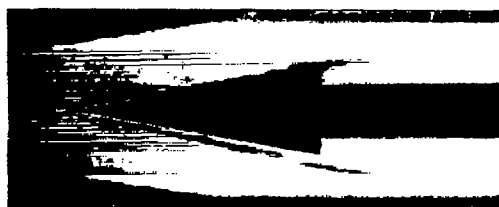
5° cone

10° cone

(a) $M_{le} = 16.1.$ L-57-2706

Figure 10.- Schlieren photographs of test models.

Flat plate

5° wedge

10° wedge
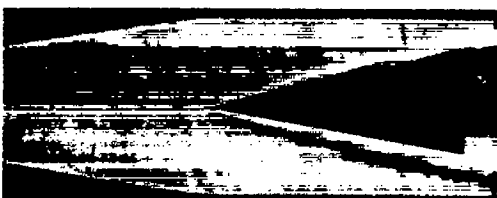
5° cone
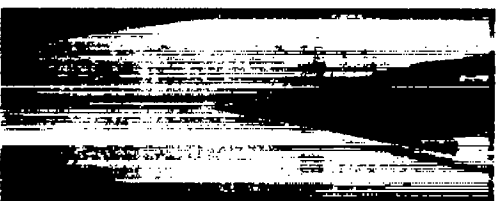
10° cone

(b) $M_{le} = 17.3.$ L-57-2707

Figure 10.- Concluded.
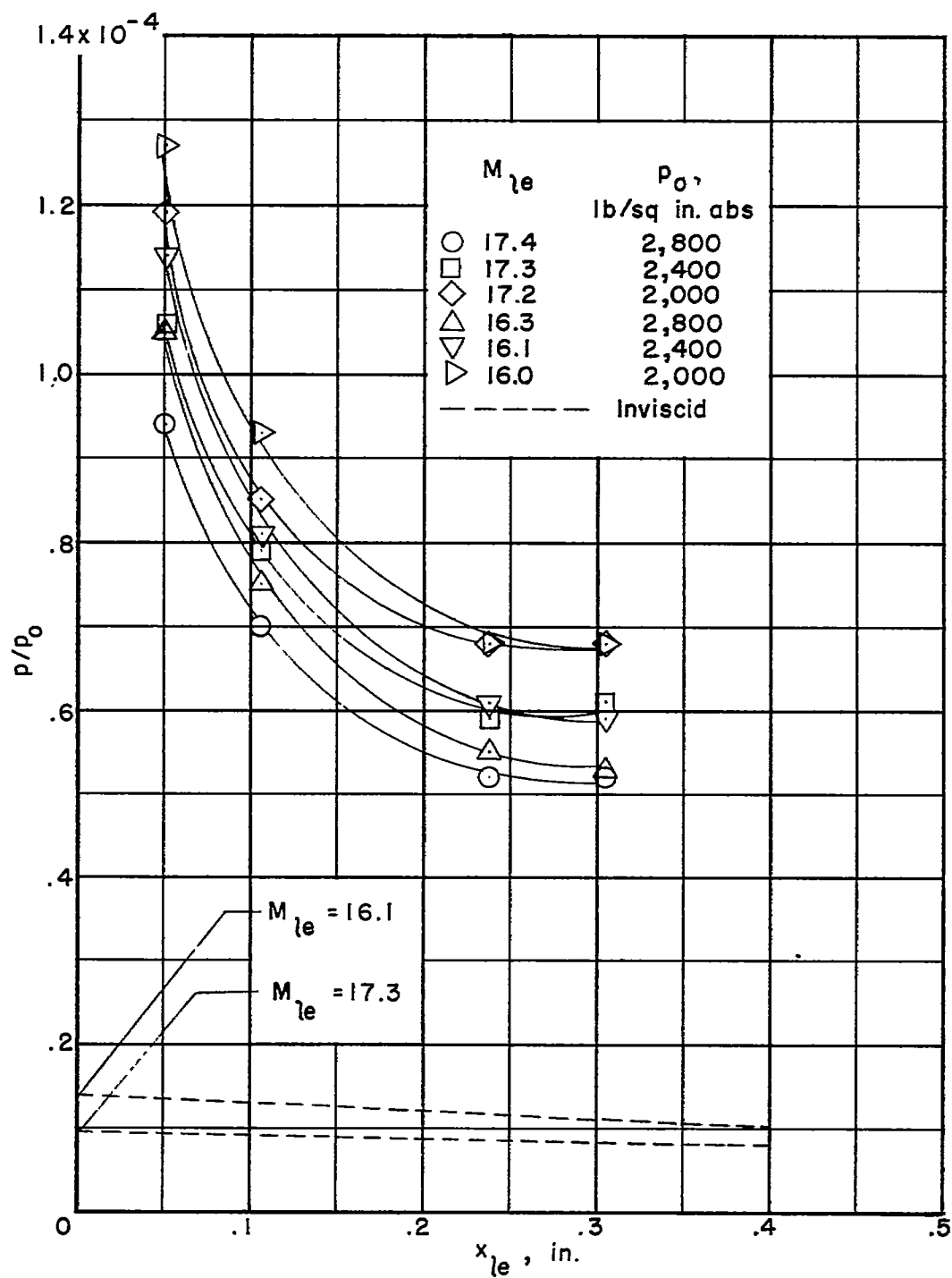
Figure 11.- Variation of ratio of surface pressure to stagnation pressure with distance from leading edge of flat plate.
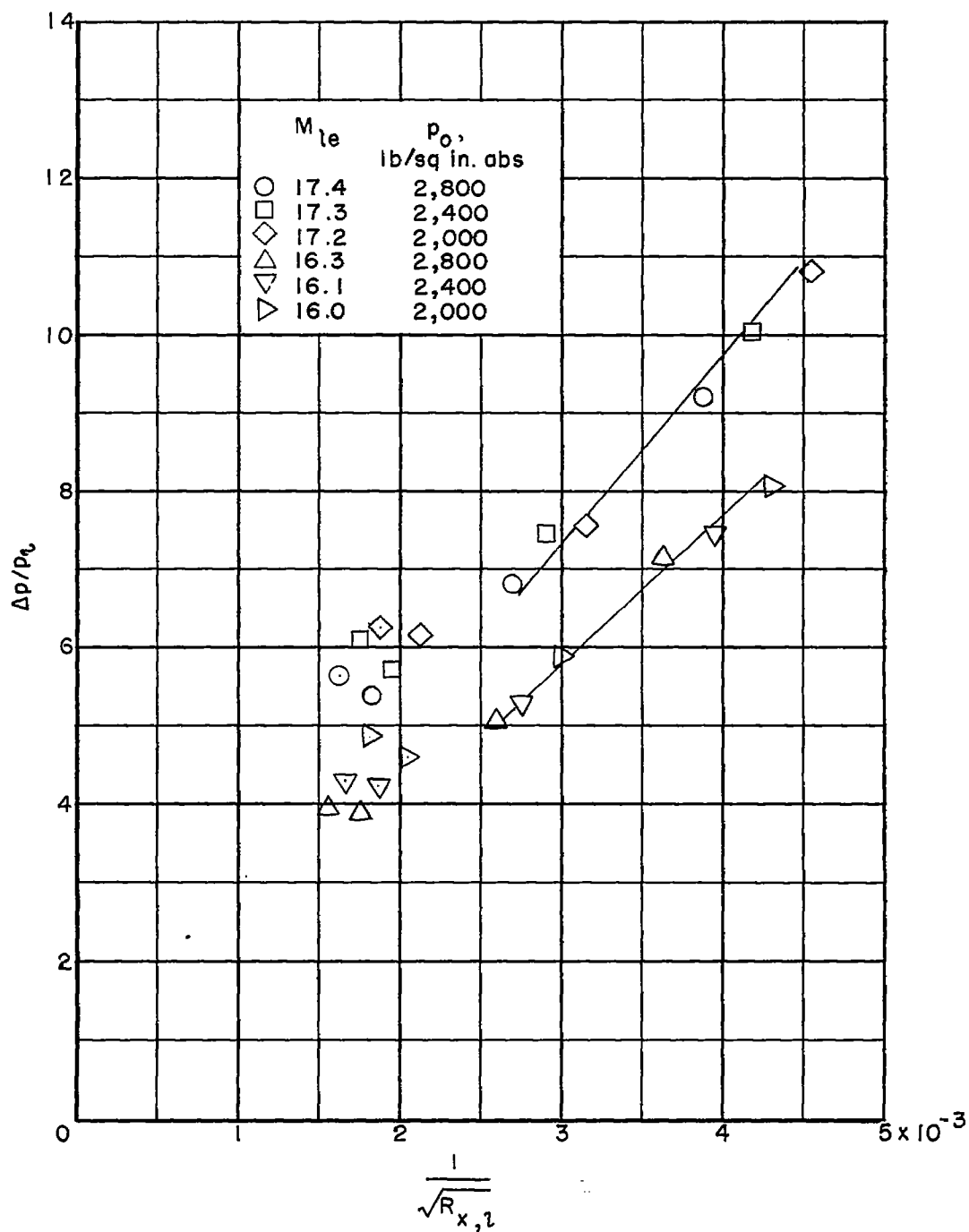
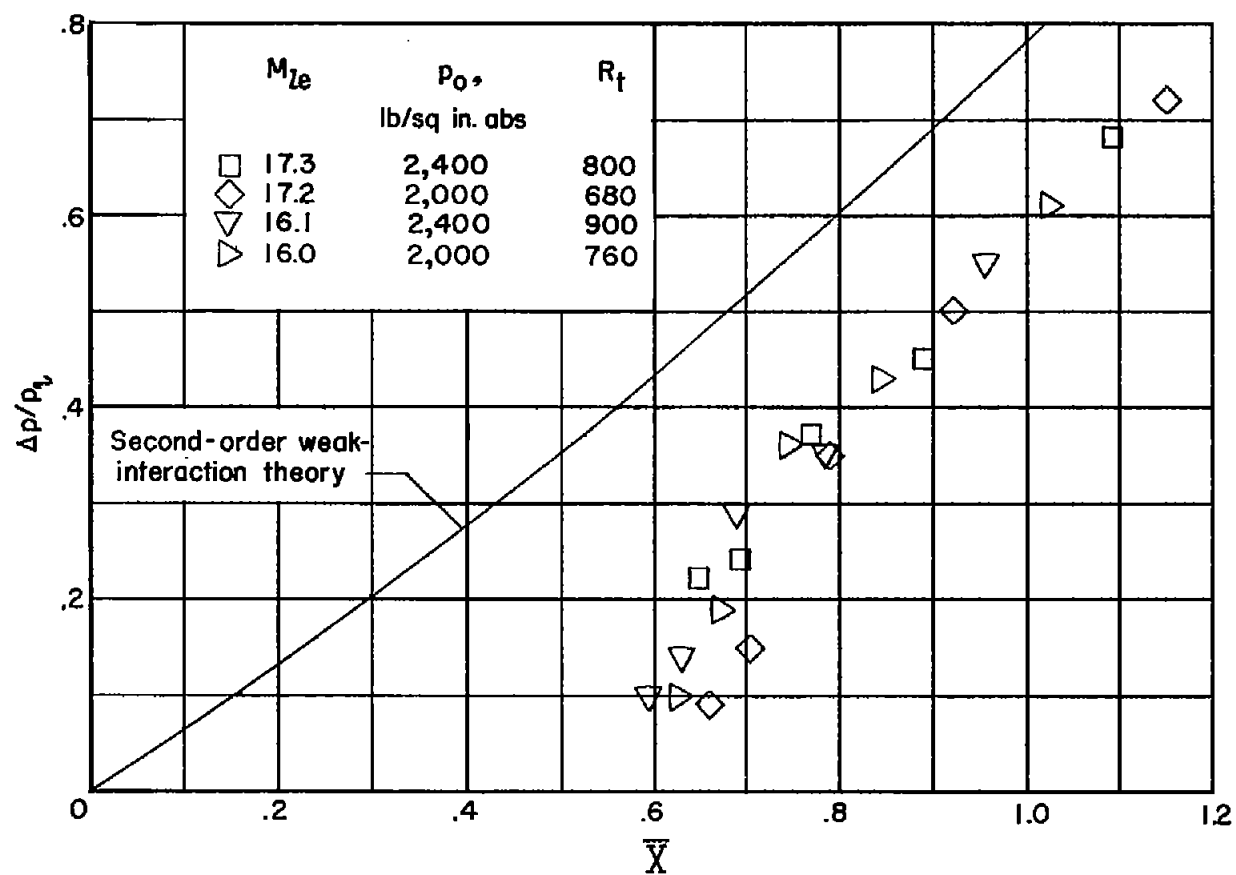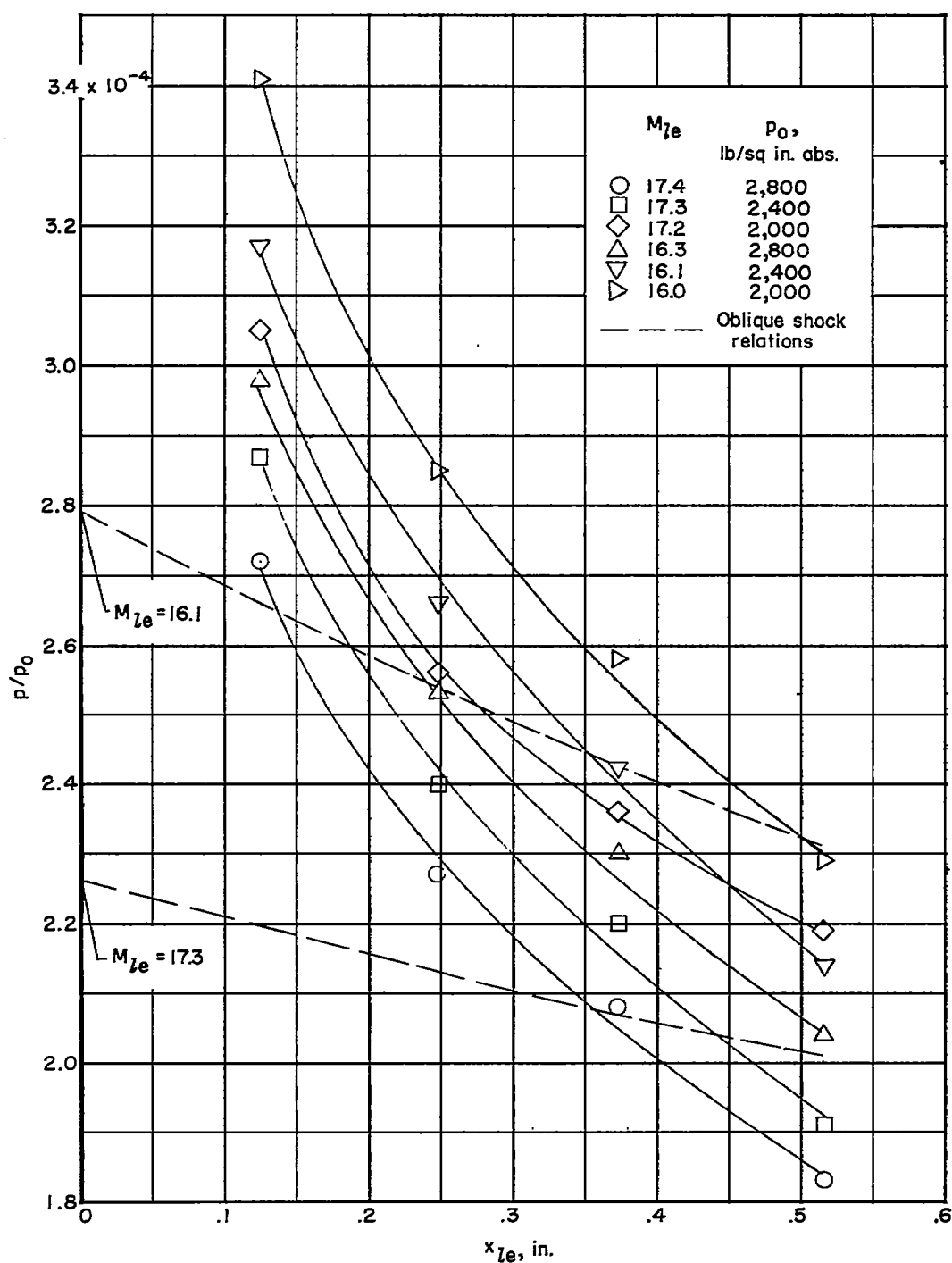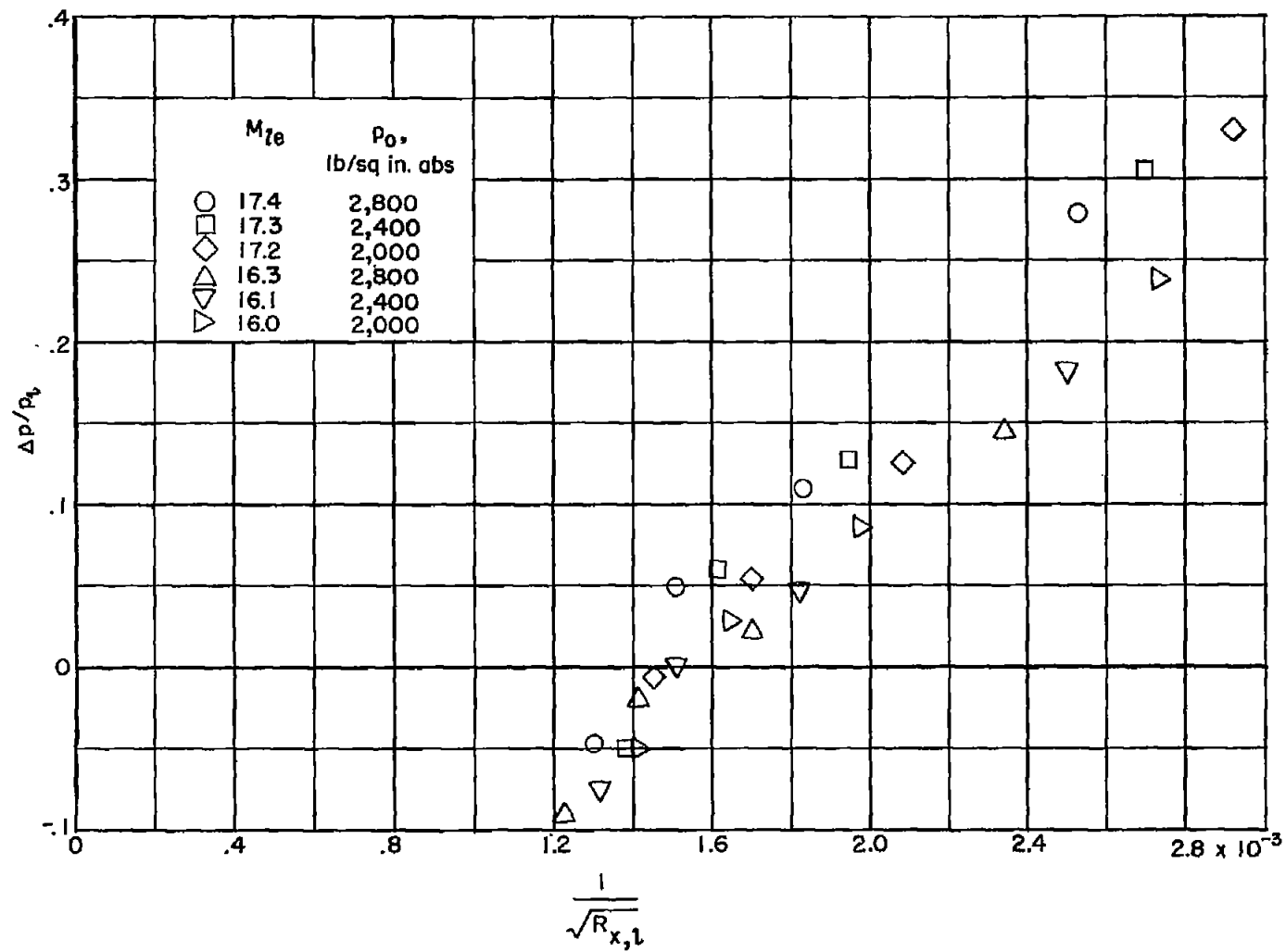Figure 12.- Induced-static-pressure ratio plotted against $1/\sqrt{R_{x,l}}$ for flat plate.
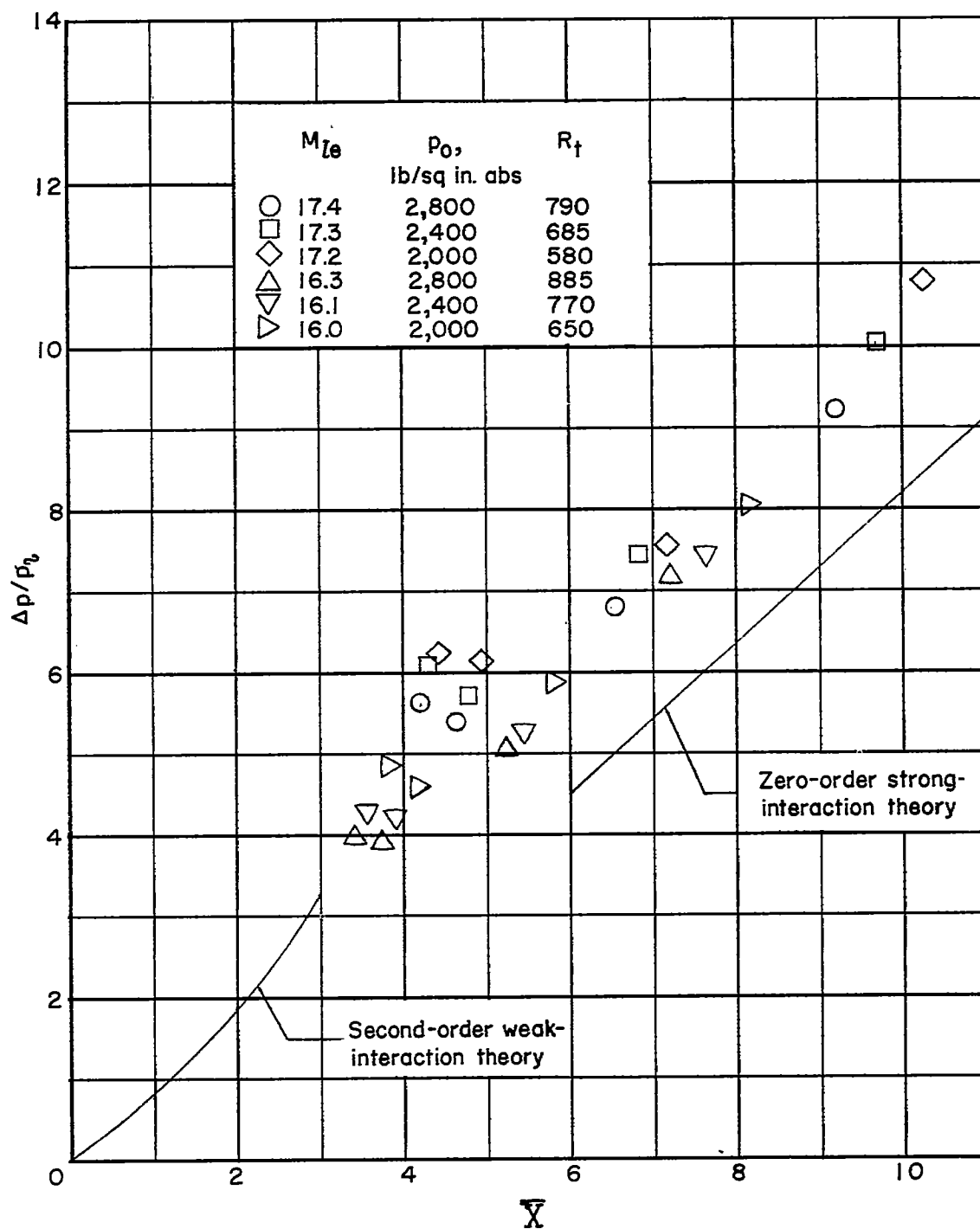
Figure 13.- Induced-static-pressure ratio plotted against $\bar{X}$ for flat plate.
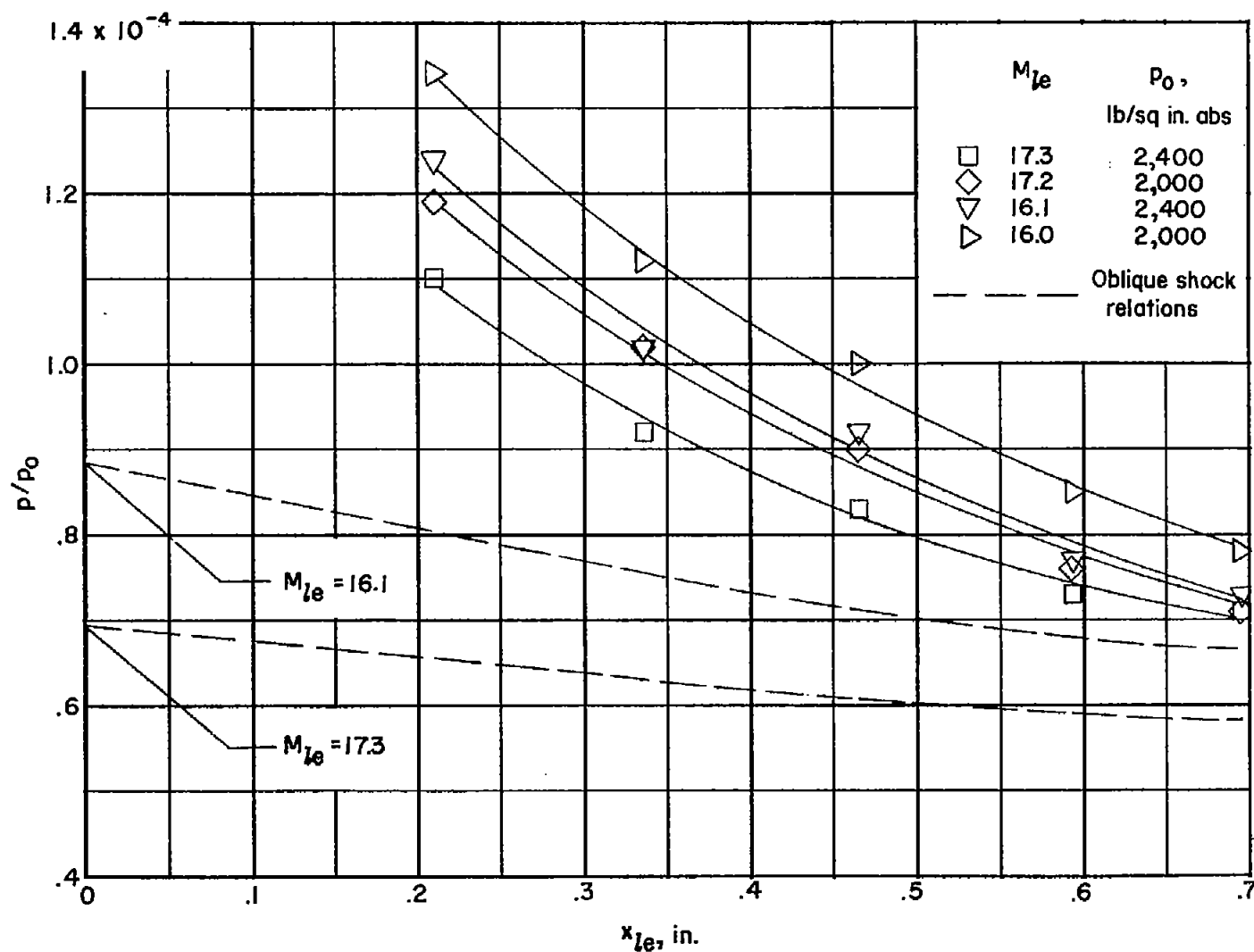
Figure 14.- Variation of ratio of surface pressure to stagnation pressure with distance from leading edge of 5° wedge.
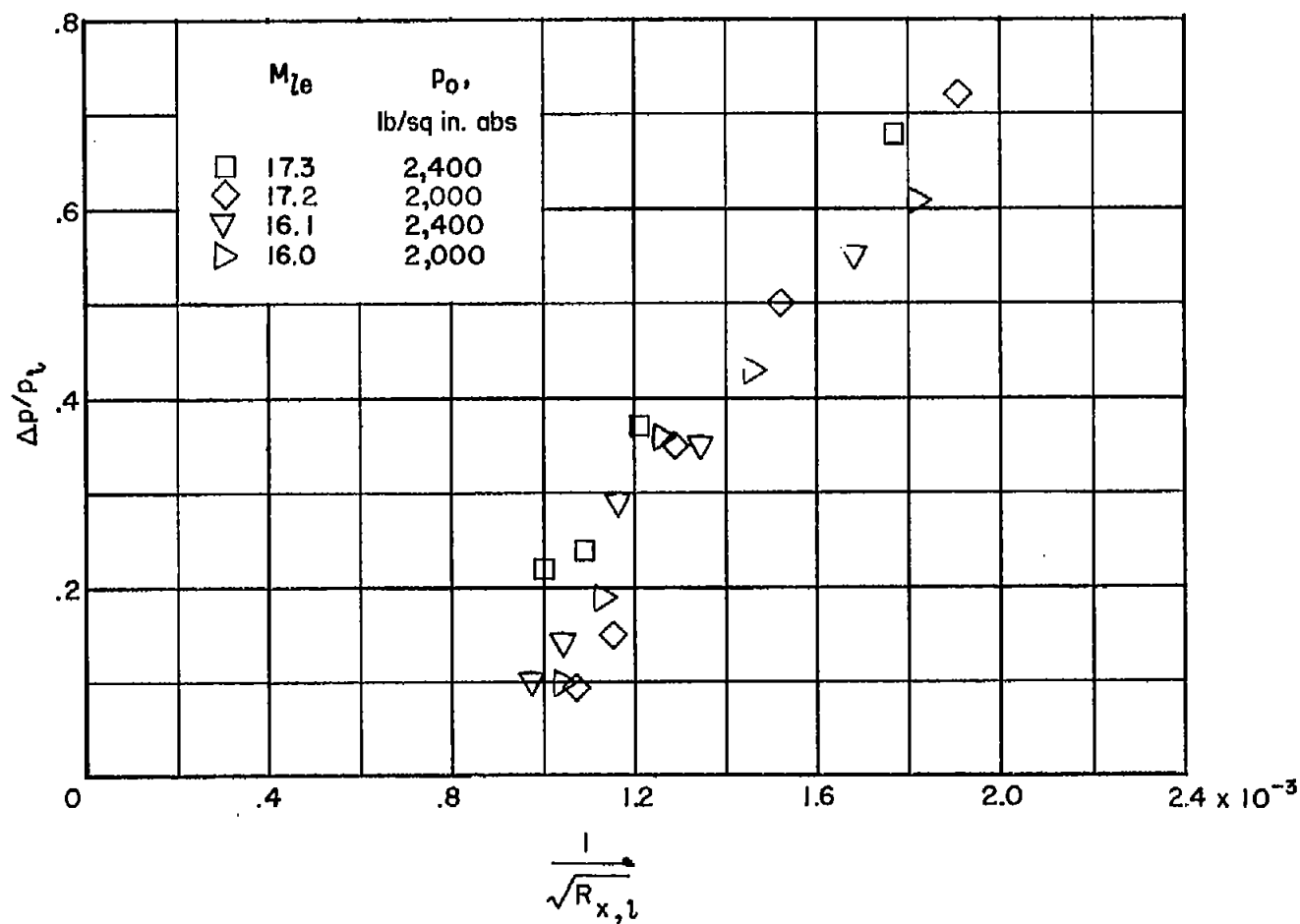
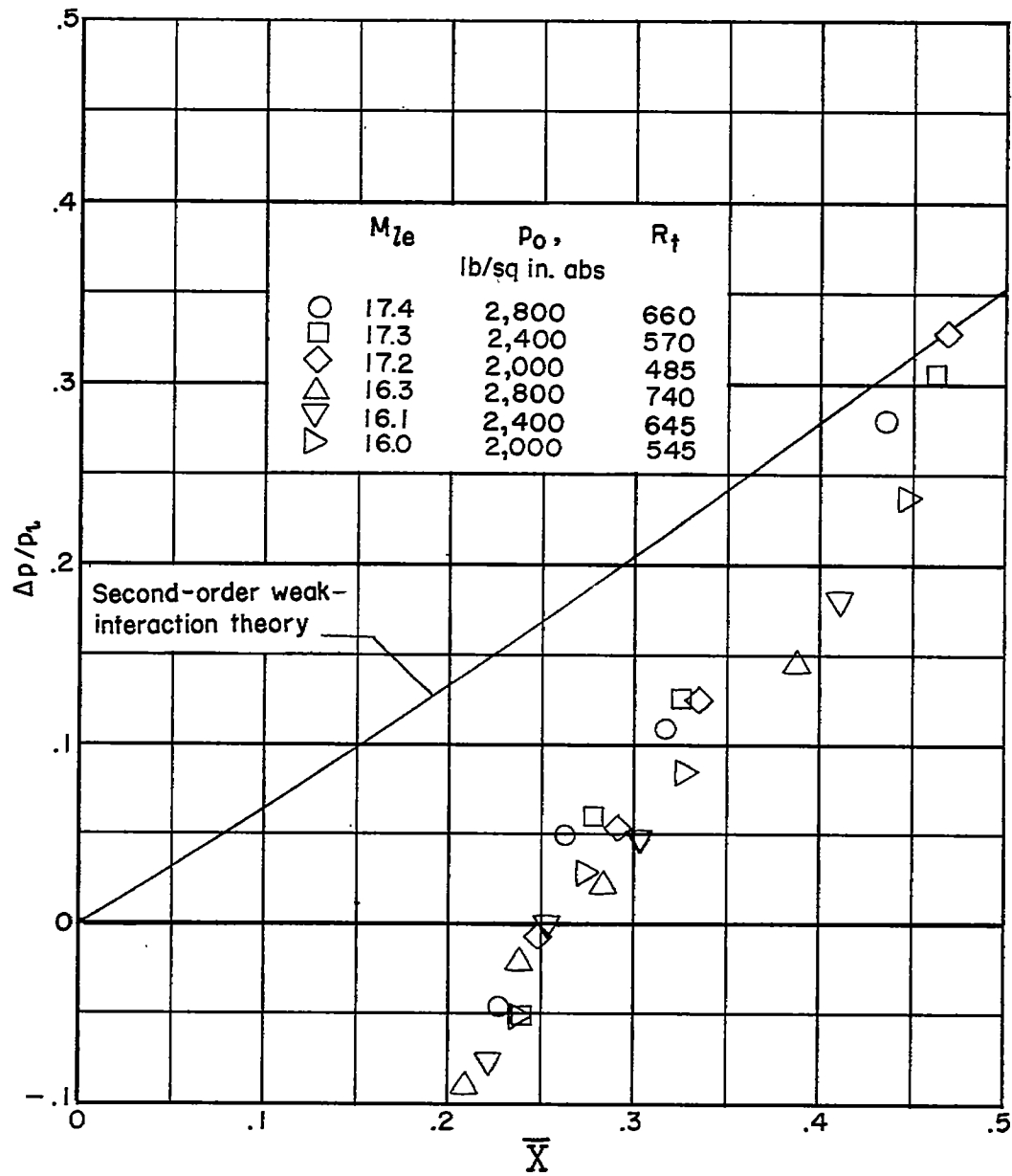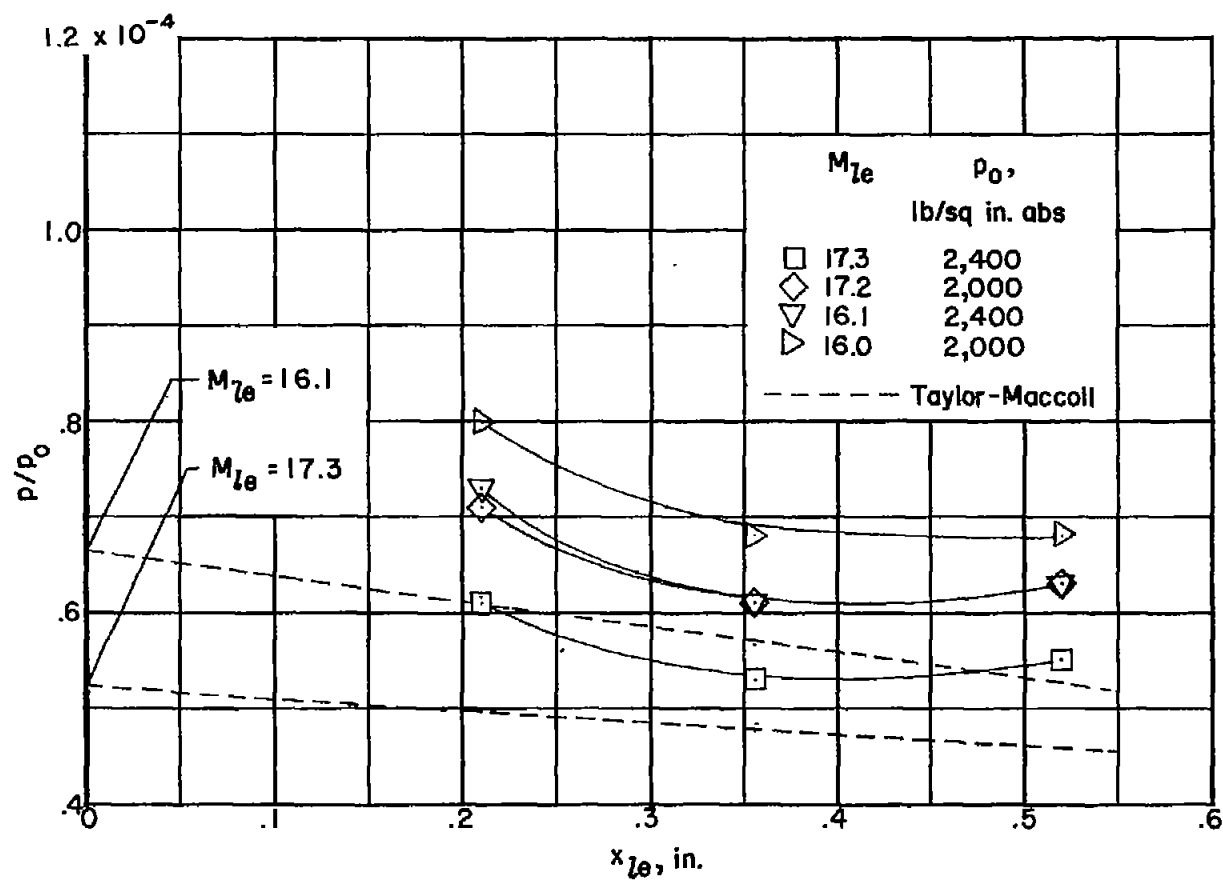Figure 15.- Induced-static-pressure ratio plotted against $1/\sqrt{R_{x,l}}$ for 5° wedge.

M_{le}	p_o, lb/sq in. abs	R_t
□ 17.3	2,400	800
◇ 17.2	2,000	680
▽ 16.1	2,400	900
▷ 16.0	2,000	760

Second-order weak-interaction theory

Figure 16.- Induced-static-pressure ratio plotted against $\overline{X}$ for $5°$ wedge.

Figure 17.- Variation of ratio of surface pressure to stagnation pressure with distance from leading edge of $10°$ wedge.

Figure 18.- Induced-static-pressure ratio plotted against $1/\sqrt{R_{x,l}}$ for 10° wedge.

Figure 19.- Induced-static-pressure ratio plotted against $\overline{X}$ for 10° wedge.

Figure 20.- Variation of ratio of surface pressure to stagnation pressure ratio with distance from leading edge of 5° cone.
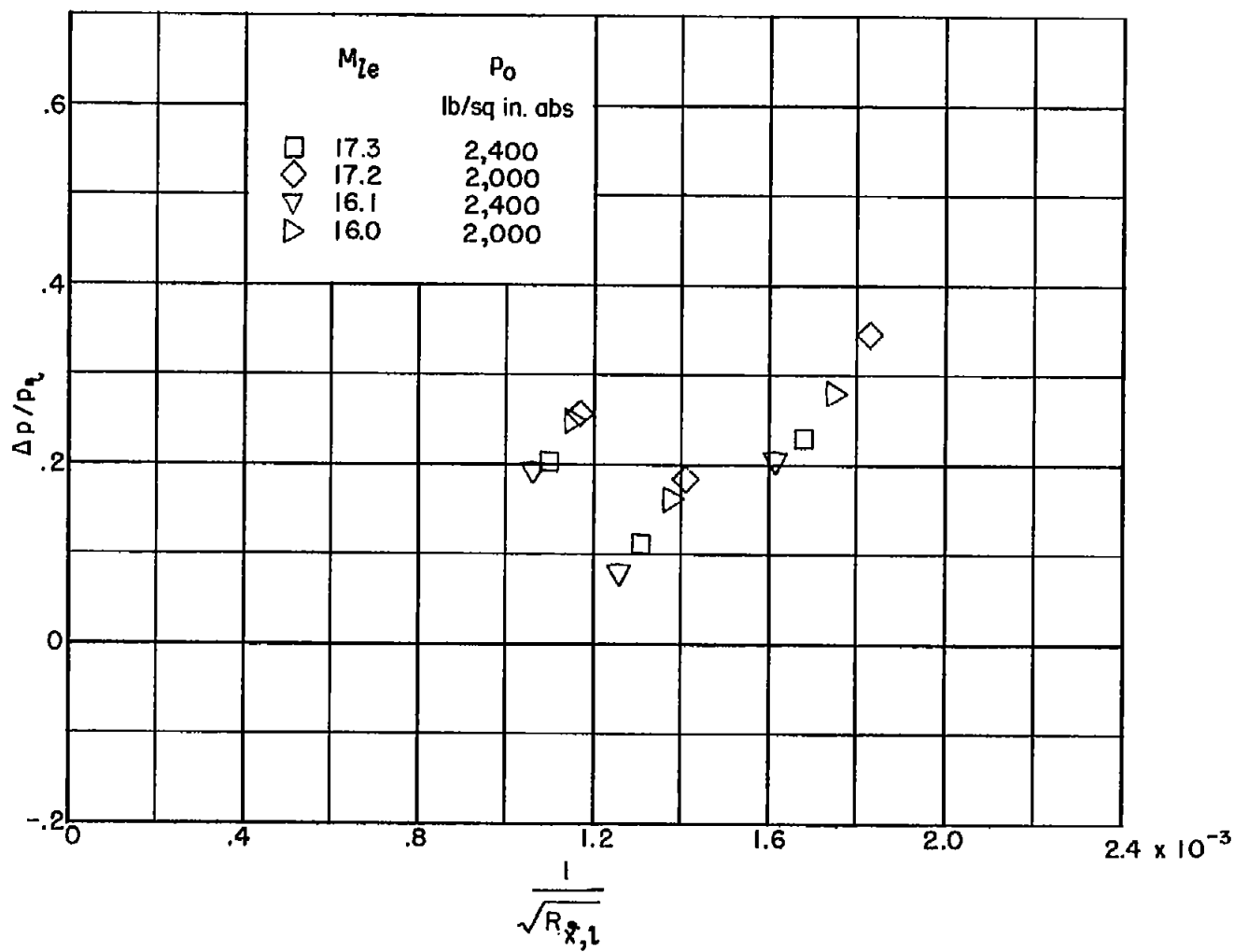
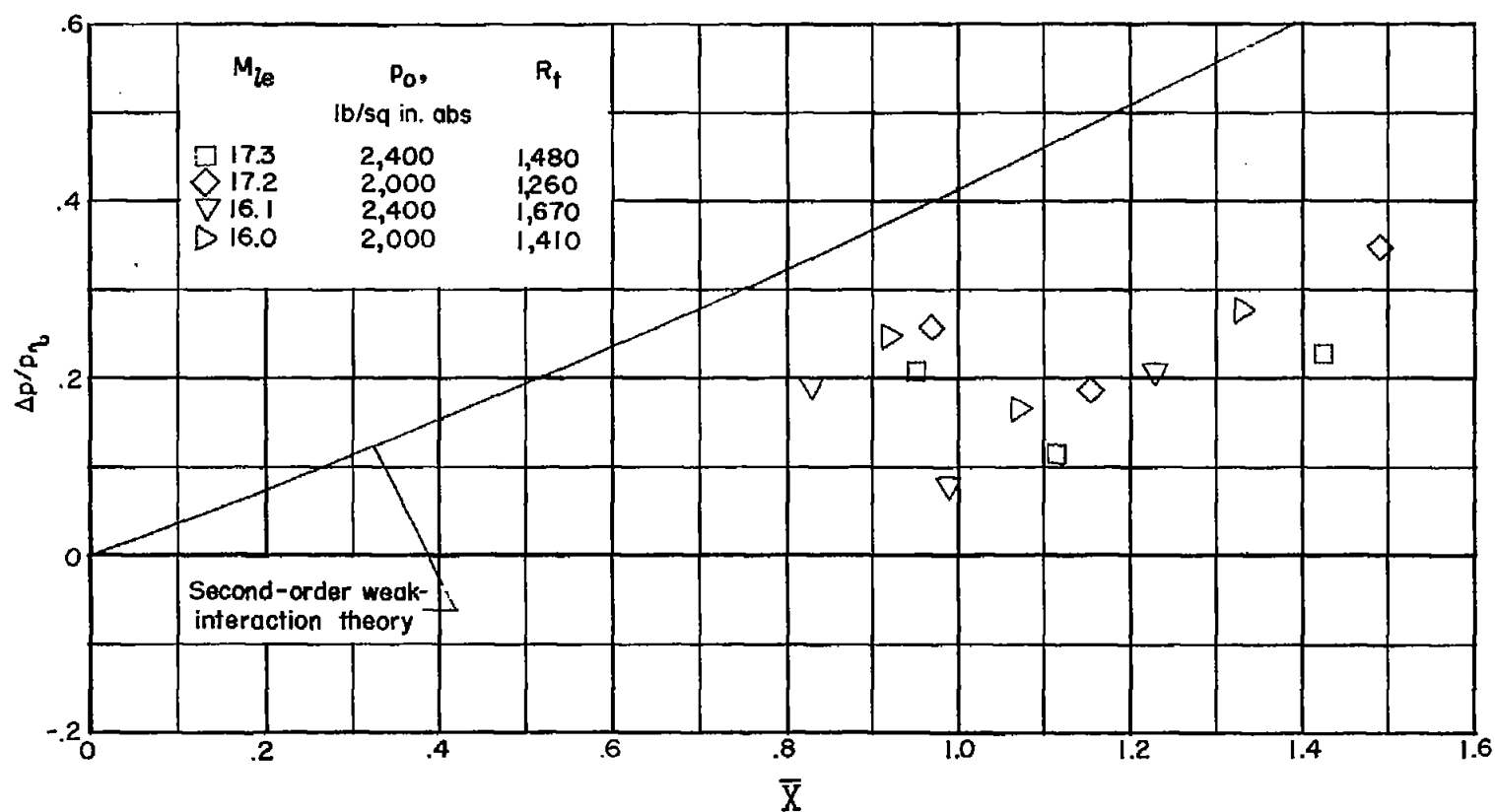Figure 21.- Induced-static-pressure ratio plotted against $1/\sqrt{R_{x,l}}$ for $5°$ cone.

Figure 22.- Induced-static-pressure ratio plotted against $\bar{X}$ for 5° cone.
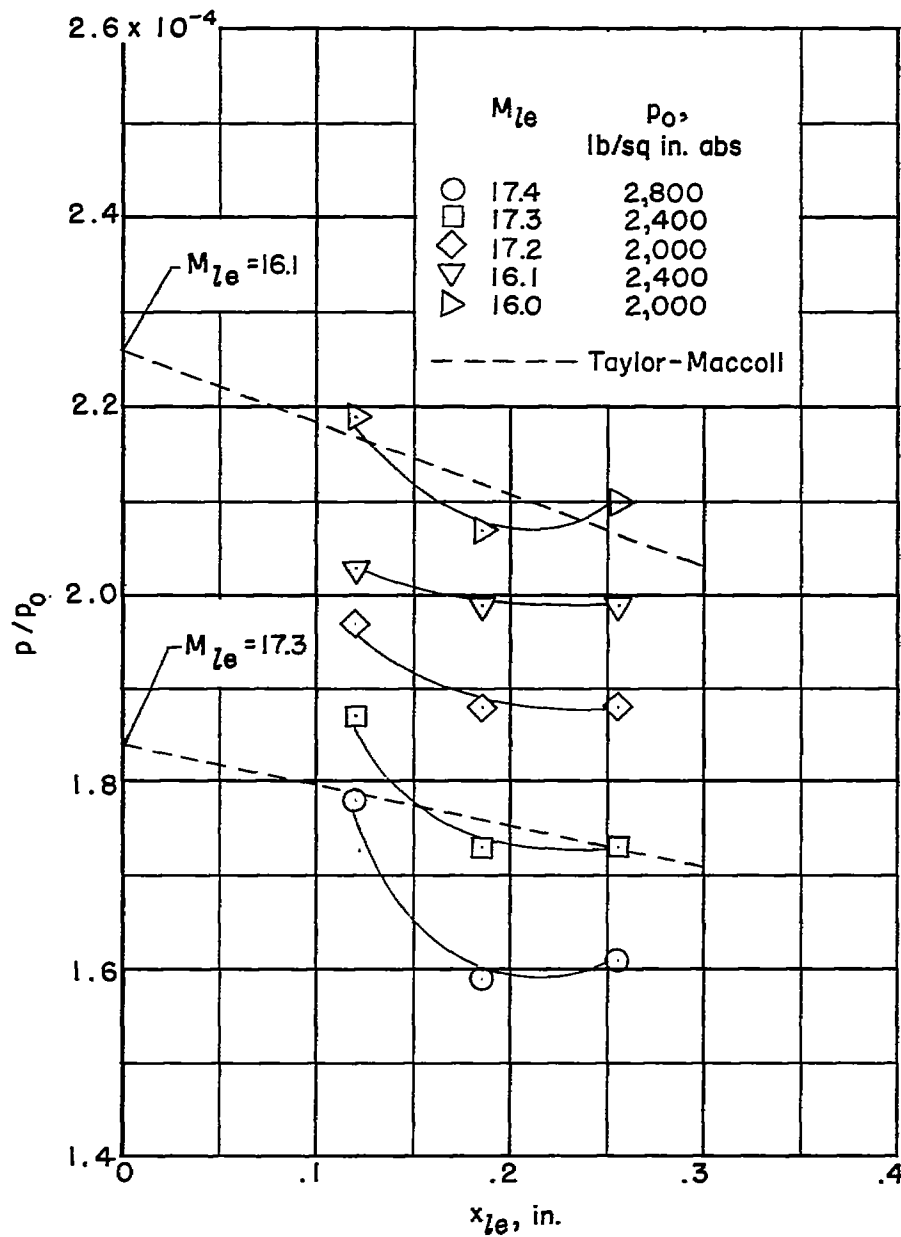
Figure 23.- Variation of ratio of surface pressure to stagnation pressure with distance from leading edge of 10° cone.
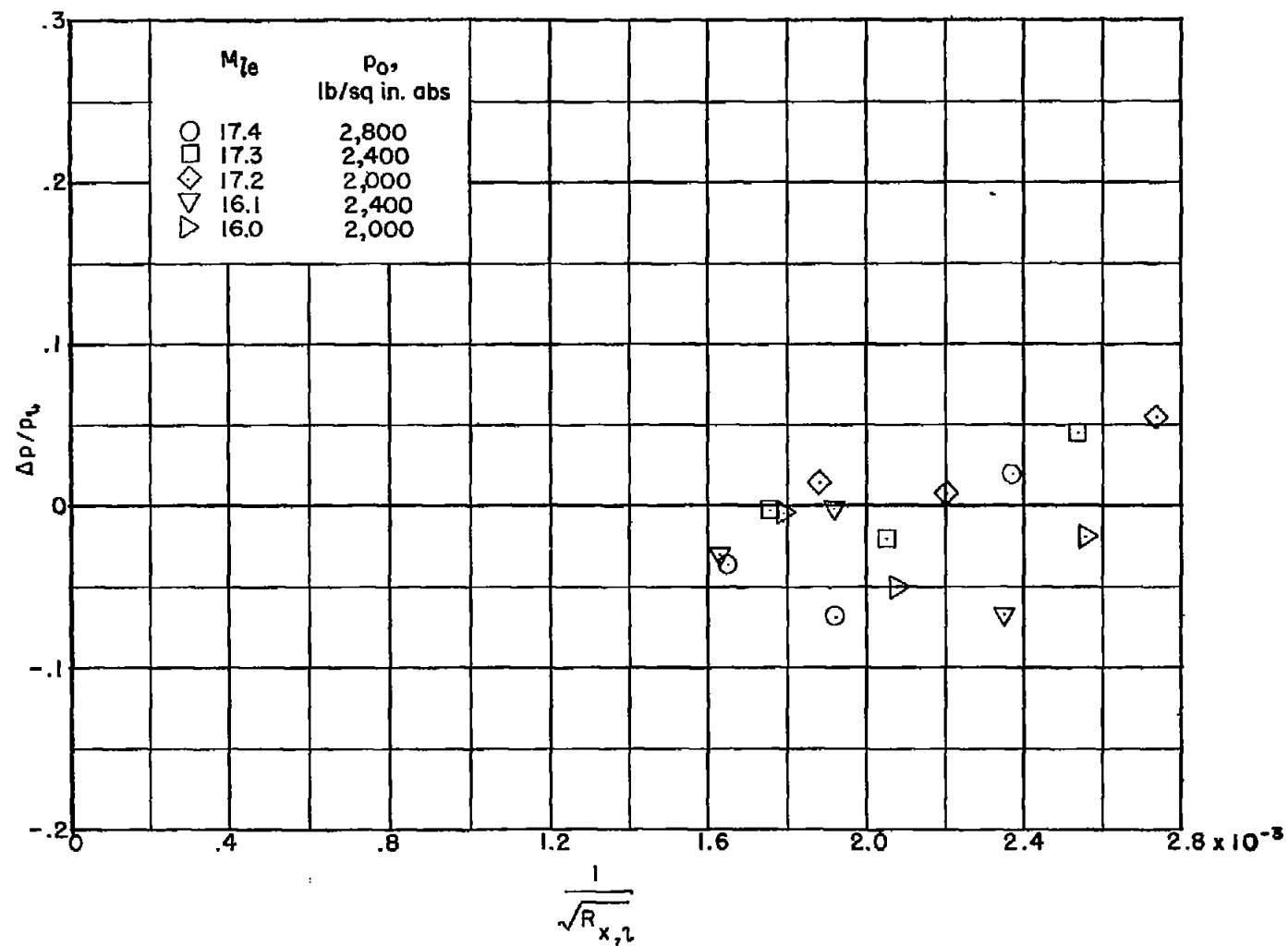
Figure 24.- Induced-static-pressure ratio plotted against $1/\sqrt{R_{x,l}}$ for 10° cone.
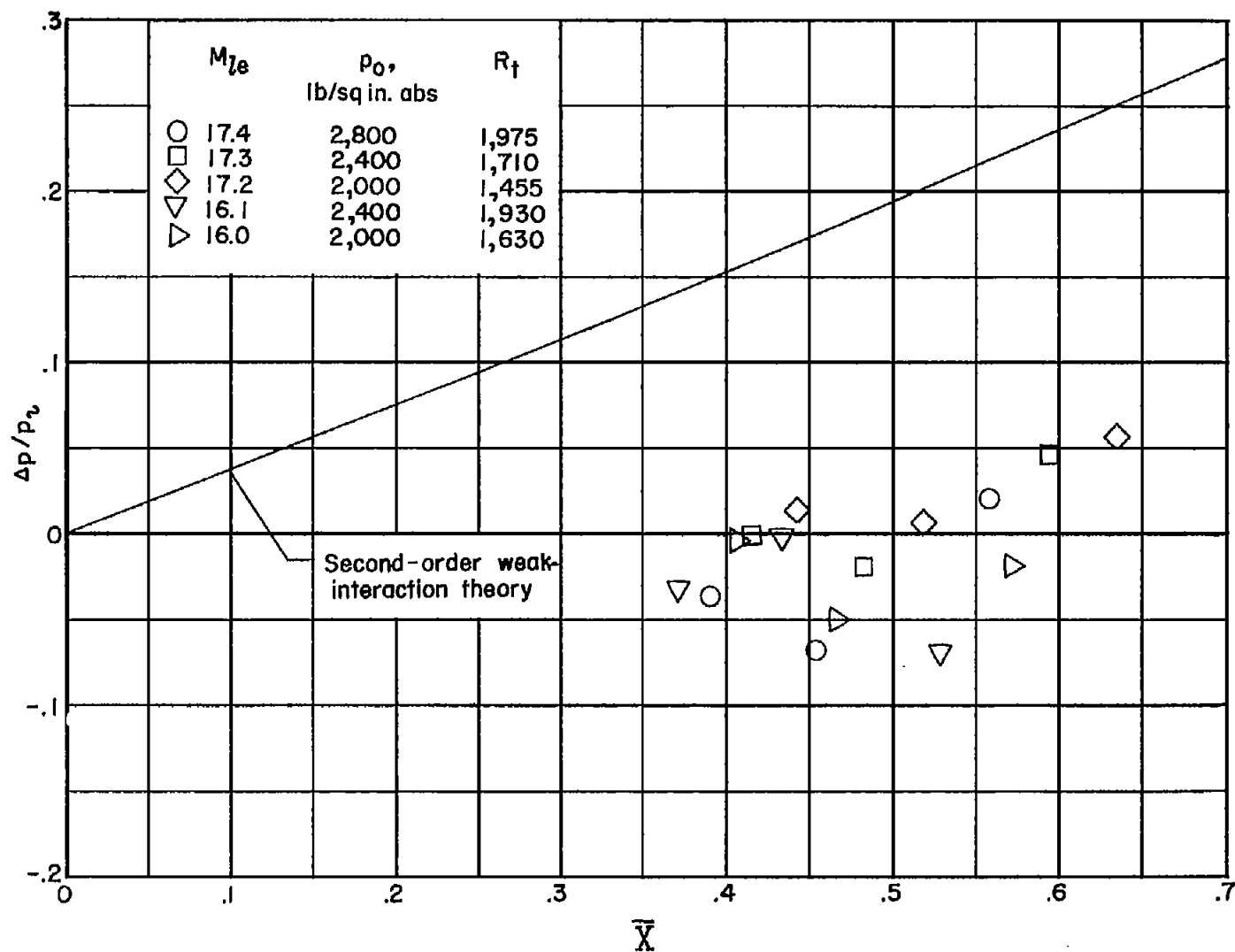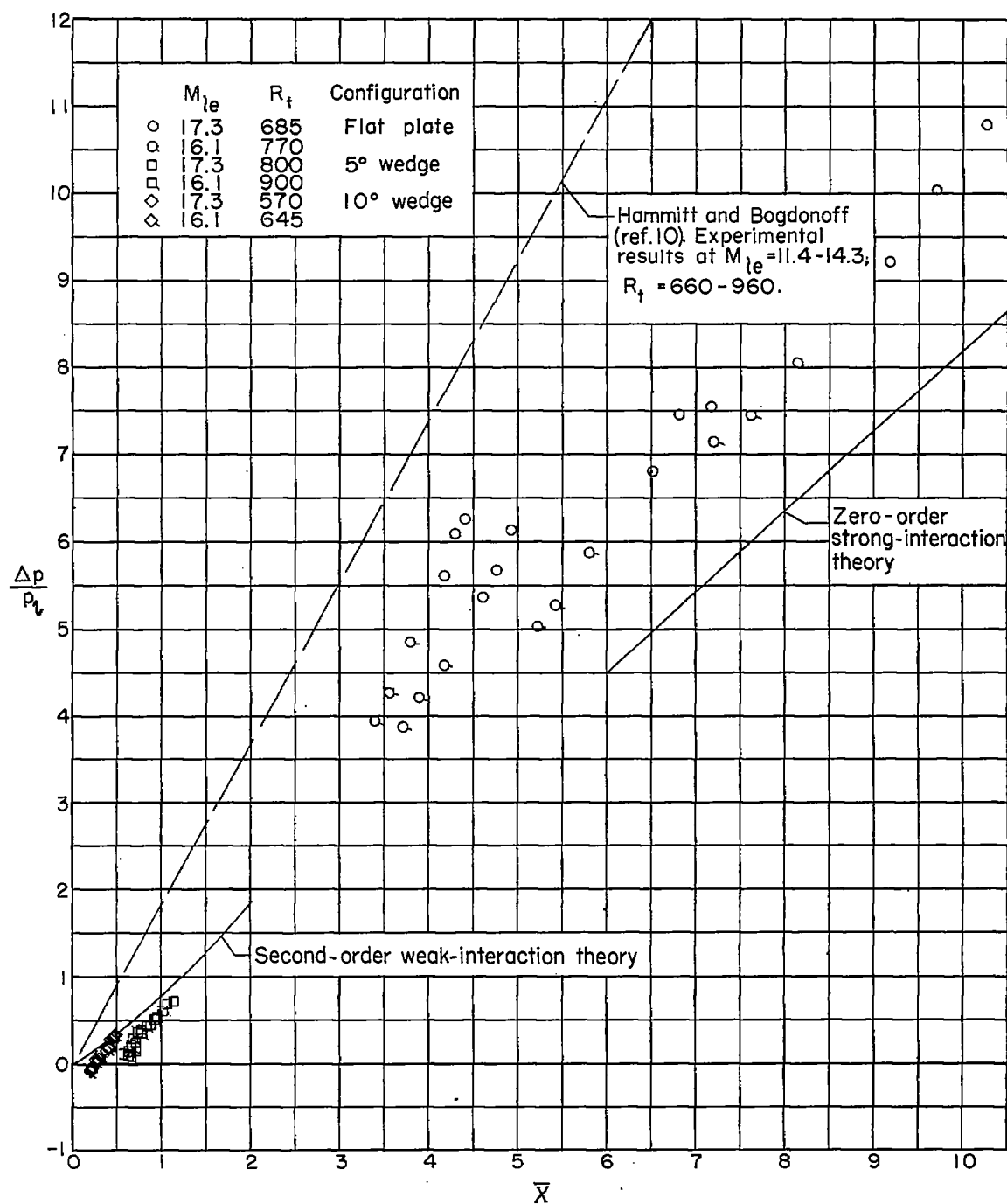
M_{le}	p_0, lb/sq in. abs	R_t
○ 17.4	2,800	1,975
□ 17.3	2,400	1,710
◇ 17.2	2,000	1,455
▽ 16.1	2,400	1,930
▷ 16.0	2,000	1,630

Second-order weak-
interaction theory

$\Delta p/p_t$

$\overline{X}$

Figure 25.- Induced-static-pressure ratio plotted against $\overline{X}$ for 10° cone.

Figure 26.- Induced-static-pressure ratio plotted against $\overline{X}$ for flat plate, 5° wedge, and 10° wedge.